UNIVERSITY OF CALIFORNIA

Los Angeles

In situ Scanning Electron Microscopy Based Uniaxial Compression of Sub-Micrometer-Size Transition-Metal Carbide Single-Crystalline Pillars

A dissertation submitted in partial satisfaction

of the requirements for the degree

Doctor of Philosophy in Mechanical Engineering

by

Angel Cortez Aleman

2023

ABSTRACT OF THE DISSERTATION

In situ Scanning Electron Microscopy Based Uniaxial Compression of Sub-Micrometer-Size Transition-Metal Carbide Single-Crystalline Pillars

by

Angel Cortez Aleman
Doctor of Philosophy in Mechanical Engineering
University of California, Los Angeles, 2023
Professor Suneel Kumar Kodambaka, Co-Chair
Professor Nasr M. Ghoniem, Co-Chair

The B1-structured group 5 transition metal carbides (VC, NbC, and TaC) are refractory compounds that exhibit a remarkable mixture of ionic, covalent, and metallic bonding. They are attractive materials for numerous and diverse applications and are of great interest to the scientific community. In this dissertation I investigated their mechanical behavior, observed plasticity at room-temperature, measured anisotropic yield strengths as a function of crystal (pillar) size, and determined their deformation mechanism. With *in situ* scanning electron microscopy based uniaxial microcompression testing, I show that single-crystalline sub-micrometer-size transition-metal carbides exhibit orientation- and size-dependent room-temperature plasticity. I find that for all the group 5 carbides, the yield strength increases with decreasing pillar size. For NbC(001) pillars, I observed that the extent of plastic deformation

increases with increasing diameter. Surprisingly, in the smallest pillars the $\{110\}\langle 1\bar{1}0\rangle$ slip system is activated and for relatively larger pillars, the $\{111\}\langle 1\bar{1}0\rangle$ slip system is activated, indicating a transition in slip system based on size. I show that the largest pillars sustain extended plastic deformation. For VC, I present the microcompression test results of 001, 110, and 111 crystal orientations, where I have identified the operation of up to three slip systems dependent on the crystal orientation. I find that the mechanical behavior for VC(001) is similar to that of NbC(001) with a size-dependent transition in the operating slip systems. In VC(110) pillars, for all sizes, I observed minimal local plastic deformation followed by local fracture resulting in several large slip bands and is therefore described as brittle. In VC(111), the pillars exhibit size-dependent plasticity that increases with increasing diameter, however to a lesser extent than VC(001). For TaC, I investigated the mechanical responses of 110- and 111- oriented pillars. Similar to VC(110), the TaC(110) pillars are brittle. The TaC(111) pillars exhibit plasticity, however, to a lesser extent than in VC(111) pillars. Surprisingly, the largest diameter TaC(111) pillars are brittle. I have identified the operation of two slip systems dependent on the crystal orientation and pillar diameter, and also the observation of a transition in slip system for both orientations. My results also point to the exciting possibility of designing refractory TMCs with superior plasticity by optimizing the grain sizes, orientations, and compositions that promote the activation of desired slip systems.

The dissertation of Angel Cortez Aleman is approved.

Jenn-Ming Yang

Vijay Gupta

Suneel Kumar Kodambaka, Committee Co-Chair

Nasr M. Ghoniem, Committee Co-Chair

University of California, Los Angeles

2023

Dedicated to my mother

TABLE OF CONTENTS

LIST OF FIGURES

LIST OF TABLES

ACKNOWLEDGEMENTS

I want to express my gratitude to the people who helped me along my journey at UCLA. This thesis was completed with the collaboration, support, and advice from many members of the UCLA community whom I have been fortunate to meet as a PhD student.

I give my sincerest gratitude to my advisor Professor Suneel Kodambaka for allowing me the opportunity to work in his group, for his invaluable guidance and continuous support throughout this project, for being patient, and supportive of my academic and career goals. I genuinely thank my thesis committee members: Professors Nasr Ghoniem, Vijay Gupta, and Jenn-Ming Yang for their advice and support during my PhD study and taking the time to review the work presented here. I thank all of the faculty and staff in the Mechanical and Aerospace Engineering and Materials Science and Engineering departments with whom I had the opportunity to work with via teaching assignments, research and academic topics, and outreach programs. Special thanks to the student affairs officers that guided me through the department mazes and paperwork.

I gratefully acknowledge that all of the research projects presented here were supported by the Air Force Office of Scientific Research (AFOSR, Dr. Ali Sayir) under Grant # FA9550-14-1-0106 and # FA9550-18-1-0050 and the National Science Foundation (NSF CMMI) grant #1563427 (Dr. Kara Peters). I acknowledge the use of instruments at the Electron Imaging Center for NanoMachines (EICN) that are housed in the California NanoSystems Institute (CNSI), the Molecular Instrumentation Center at UCLA, and the Materials Science and Engineering department and UCLA. I thank Mr. Noah Bodzin and the Nanoelectronics Research Facility (NRF) that is part of the Nanofabrication Lab (NanoLab) in the UCLA Henry Samueli School of Engineering for assistance with the FEI Nova 600 SEM/FIB dual system.

The Kodambaka Science group has trained many scientists over the years, and I am grateful to my colleagues whom I had the pleasure of working with. Drs.: Koichi Tanaka, Hicham Zaid, Aditya Deshpande, Pedro Arias, Mr. Josh Fankhauser, and Abbas Ebnonnasir: I thank you all for our valuable collaborations. I thank Sidney Tran, Yu-An Chung, Koki Hojo, Tomoyasu Watanabe, and Akshara Aditya for all of the insightful discussions and collaborations. I gratefully acknowledge Drs. Michael Liao, Chao Li, and Yekan Wang for their deep knowledge and practical skills on X-ray diffraction, which led to valuable collaborations and many insightful discussions of crystallography. I learned much from everyone, and I thank you all.

I am very grateful of having the love and support of my family and friends. I thank my mother and sister for their encouragement and reminding me to be resilient in the face of adversity. I appreciate the encouragement, advice, and inspiration that was shared from many friends.

Finally, I give my deepest gratitude to my beloved nuclear family especially my Maria. The love, support, tremendous appreciation and encouragement, motivated and fueled me to complete my study. I look forward to unraveling our future.

VITA

EDUCATION

University of California, Los Angeles 2017 – Present
Pursuing Ph.D. in Mechanical and Aerospace Engineering

RESEARCH EXPERIENCE

Graduate Student Researcher 2017 – 2023
Kodambaka *In Situ* Microscopy Lab UCLA, Los Angeles, CA

PUBLICATIONS/MANUSCRIPTS

A. Aleman, H. Zaid, B.M. Cruz, K. Tanaka, J.M. Yang, H. Kindlund, and S. Kodambaka, *Room-temperature plasticity and size-dependent mechanical responses in small-scale B1-NbC(001) single-crystals.* Acta Materialia, **221,** 2021.

A. Aleman, C. Li, H. Zaid, H. Kindlund, J. Fankhauser, S.V. Prikhodko, M.S. Goorsky, and S. Kodambaka, *Ultra-high vacuum dc magnetron sputter-deposition of epitaxial Pd(111)/Al2O3(0001) thin films.* Journal of Vacuum Science & Technology A, **36**(3), 2018.

A. Aleman, H. Zaid, K. Tanaka, J.M. Yang, H. Kindlund, and S. Kodambaka, *Anisotropic slip and size-dependent room-temperature plasticity in uniaxially compressed sub-micrometer size 001, 110, and 111-oriented B1-VC single-crystals.* (Manuscript, provisional title)

A. Aleman, K. Tanaka, H. Zaid, J.M. Yang, H. Kindlund, and S. Kodambaka, *Room-temperature anisotropic and size-dependent mechanical responses in small-scale B1-TaC single-crystals.* (Manuscript, provisional title)

K. Tanaka, P. Arias, K. Hojo, T. Watanabe, M. Liao, **A. Aleman**, H. Zaid, M. Goorsky, and S. Kodambaka, *Borazine Promoted Growth of Highly Oriented Thin Films.* Nano letters, 23 (2023).

K. Tanaka, M.E. Liao, **A. Aleman**, H. Zaid, M.S. Goorsky, S. Kodambaka, *Growth of heterolayered [cubic-TaC(111) + rhombohedral-Ta_3C_2(0001)] nanocomposite thin films on Al_2O_3(0001),* Acta Materialia 204 (2021).

H. Zaid, **A. Aleman**, S. Kodambaka, *Size-dependent yielding and strain-hardening of compositionally-enriched body-centered cubic VNbTaMoW alloy,* Scripta Materialia 178, 518-521 (2020).

H. Zaid, **A. Aleman**, K. Tanaka, C. Li, P. Berger, T. Back, J. Fankhauser, M.S. Goorsky, S. Kodambaka, *Influence of ultra-low ethylene partial pressure on microstructural and compositional evolution of sputter-deposited Zr-C thin films,* Surface and Coatings Technology 398 (2020).

K. Tanaka, **A. Aleman**, H. Zaid, M.E. Liao, K. Hojo, Y. Wang, M.S. Goorsky, S. Kodambaka, *Ultra-high vacuum dc magnetron sputter-deposition of 0001-textured trigonal α-Ta_2C/Al_2O_3(0001) thin films,* Materialia 13 (2020).

K. Tanaka, **A. Aleman**, M.E. Liao, Y. Wang, M.S. Goorsky, S. Kodambaka, *Effects of ultra-low ethylene partial pressure on microstructure and composition of reactively sputter-deposited Ta–C thin films*, Thin Solid Films 688 (2019).

K. Tanaka, J. Fankhauser, H. Zaid, **A. Aleman**, M. Sato, D. Yu, A. Ebnonnasir, C. Li, M. Kobashi, M.S. Goorsky, S. Kodambaka, *Kinetics of Zr-Al intermetallic compound formation during ultra-high vacuum magnetron sputter-deposition of Zr/Al_2O_3(0001) thin films*, Acta Mater. 152, 34-40 (2018).

CONFERENCE PRESENTATIONS

UCLA MAE IAB Open House
"*In situ* scanning electron microscopy based uniaxial compression of sub-micrometer-size NbC(001) single-crystalline pillars", Los Angeles, CA, 2019

SCSMM Spring Symposium
"*In situ* scanning electron microscopy based uniaxial compression of sub-micrometer-size NbC(001) single-crystalline pillars", 2019

AWARDS

Outstanding Teaching Assistant (University of California Los Angeles, MAE) 2020

CHAPTER 1

Introduction

B1-structured group 4 and 5 transition-metal carbides (TMCs) exhibit remarkable combination of properties due to a mixture of ionic, covalent, and metallic bonds [1, 2]. They are refractory solids with some of the highest known melting temperatures (2900 ~ 4300 K), where TaC has the highest melting point (4256 K) of the carbides just below the sublimation point of graphite (4273 K), high hardness (10-30 GPa) between alumina and diamond, good thermal and electrical conductivities, good thermomechanical and chemical properties, and excellent resistance to wear, ablation, and corrosion [1]. TMCs are attractive materials within ultra-high temperature ceramics for a wide variety of applications as hard protective coatings [3], high-temperature structural components in aerospace vehicles [2] and automobiles [3], high thermal conductivity substrates for electronic circuits, coatings for semiconductor devices, and as light emitting diodes in optoelectronics [3]. Most recently, their electrochemical properties have gained attention for applications in Li-ion and Na-ion batteries, supercapacitors, and electrocatalytic reactions (oxygen evolution and reduction reactions, and hydrogen evolution reactions) for energy storage and conversion [4]. TMCs possibly have applications as materials for magnetic storage devices and superconductors replacing current materials because of their superior properties [5, 6]. Given the application potential for TMCs, knowledge of the mechanical stabilities of these materials, especially at room-temperature, is desirable.

Until recently, TMCs have been considered to be brittle under uniaxial loading at low temperatures, even though they are known to exhibit local plasticity during room-temperature microindentation [1, 7]. They are ductile at elevated temperatures ($> 0.3T_m$, where T_m is the

melting point in Kelvin) [1]. At high temperatures, the primary slip system for B1-structured TMCs is generally expected to be {111}[110] [1]. However, studies have shown that other slip systems can be activated depending on temperature, orientation, and the transition-metal [1, 8].

1.1 Microhardness

A "brittle" solid will break in a conventional (macroscopic) mechanical test. However, when the same material is placed in a microhardness indentation test, local plastic flow can occur. It is believed that the high hardness of the carbides is intrinsic. The mobility of dislocations in the carbides is expected to be very low at room temperature due to a high Peierls stress resulting from exceptionally strong bonding in the carbides [9]. Furthermore, ionic materials that are cubic with rocksalt structure, similar to TMCs are considered brittle due to surface and volume defects [10].

The plastic nature of the microhardness impression in TiC was demonstrated by authors of Ref. [11], where slip steps on the inside of the impression were detected by electron microscopy. Additionally, the anisotropic microhardness of TiC, ZrC, VC, and NbC have been demonstrated by Hannink *et al*. [8]. These findings indicate that these TMCs have anisotropic mechanical properties and dislocations participate in the room-temperature deformation as observed in microhardness tests.

1.2 Carbon to metal ratio

Transition metals of groups 4 and 5 can easily form monocarbide compounds with a wide homogeneity range. The chemical formula widely used is MeC_x, where Me represents a transition metal, C is carbon, and x is the carbon-to-metal ratio. The value of the carbon ratio (x)

varies from approximately 0.5 to 0.97. As such, the monocarbides are carbon-deficient, nonstoichiometric compounds, having several percentage vacancies. These vacancies affect the mechanical, transport, and many other properties. Some properties (hardness, electrical, and magnetic etc.) are extremely sensitive to vacancies on both metal and nonmetal lattice sites. The insidious factor of porosity contributes to a detriment on the mechanical properties because of its adverse impact as the porosity increases in the sintered samples [1].

Interestingly, Figure 1.1 shows how the hardness of TMCs depend on carbon content. From the figure it is apparent that hardness of group 4 carbides increases almost linearly with carbon content up to stoichiometry while the hardness of group 5 carbides decreases after a carbon-to-metal ratio of approximately x = 0.82 [2].

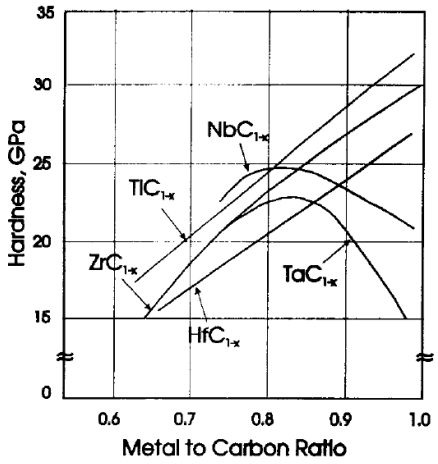

Figure 1.1: Hardness of TMCs as a function of the metal-to-carbon ratio, adapted from Ref. [3].

1.3 Microcompression

The extremely high melting points of the carbides made them difficult to prepare in single crystal form and all mechanical property measurements reported prior to 1960 were on hot-pressed or sintered carbides. These specimens suffered from impurity segregation at grain

boundaries and poorly characterized carbon-to-metal ratios calling into question the transport and mechanical properties. Fracture was common and dislocation studies were impractical. Then the advent of several crystal-growth techniques was established and successfully applied to carbides to pave the way for reliable studies [1].

Microcompression testing has attracted considerable interest in the study of size effects on mechanical properties [12-15]. Microcompression studies in experiments and simulations have shown differences in mechanical properties of materials at the sub-micrometer scale compared to their bulk counterparts [14-16]. Therefore, crystal size, orientation [17, 18], composition [1], and choice of microstructure must be considered when comparing the mechanical properties of materials.

1.4 Motivation

Although it has been shown that microcompression can be successfully employed to suppress cracking due to the small sample dimensions, little data is available in the literature on experiments with single crystal TMCs. Microcompression tests conducted on carefully prepared TMC single-crystals of different sizes can provide new insights into the mechanical behavior of this class of materials.

Furthermore, while TMCs have been considered promising materials for a variety of structural applications, their practical use has, however, been limited because relatively little is known concerning the fundamental mechanisms controlling their mechanical behavior. Understanding the atomic-scale processes underlying deformation in TMCs can, *in principle*, open opportunities for their use at low-temperatures. This requires the realization, and further, the design of low-temperature plasticity in TMCs.

Therefore, the motivation of my research is the fundamental understanding of the size- and orientation-dependent mechanical behavior of the TMCs. This information will help develop an understanding of the mechanical behavior and provide insight into the intrinsic plasticity in this class of materials.

1.5 Purpose of the Study (Hypothesis)

TMCs are known to be ductile at elevated temperatures and are considered to be brittle at low temperatures. This has limited their use as structural materials for room temperature applications. The underlying hypothesis is that TMCs are intrinsically ductile and the observed brittleness in this class of materials is due to extrinsic defects such as voids, porosity, and surface cracks. Such extrinsic defects are a direct result of the manufacturing processes and large sample sizes. To validate this hypothesis, single-crystalline pillars of group 5 TMCs (VC, NbC, and TaC) of desired orientations and crystal sizes will be fabricated. Then their intrinsic plasticity should manifest at the small scale because significantly less amounts of defects (internal and external) are present.

1.6 Research Objectives

In this dissertation, I have completed the following tasks:

Task 1: Microfabrication of TMC single-crystalline pillars via focused ion-beam (FIB) milling of bulk crystals

Task 2: *In situ* microcompression testing of TMC pillars

Task 3: Determined the mechanical behavior for up to three low-index orientations: yield strength, extent of plasticity, and deformation mechanism

Sub-micrometer single-crystalline, with up to three unique low-index crystal orientations, TMC pillars that are substoichiometric with diameters in the range of ~250 - 750 nm are fabricated by FIB milling. Then, their mechanical behavior is determined as a function of size and crystal orientation using *in situ* scanning electron microscopy (SEM) based microcompression tests. From the compression data, I determined the yield strength, extent of plasticity prior to fracture, and the active slip systems that are controlling the mechanical deformation.

In summary, cubic rocksalt structured group 5 TMCs are ultra-high melting temperature ceramics with high hardness and intrinsic plasticity. Their mechanical properties make them attractive materials for the aerospace industry and many other applications. Single-crystalline pillars of group 5 TMCs (VC, NbC, and TaC) of three unique orientations and sub-micrometer sizes are studied.

1.7 Brief summary of results

In chapter 3, I present results from *in situ* microcompression tests of NbC(001) pillars at room temperature. This work is published in *Acta Materialia*, **221**, 117384 (2021). Using a combination of X-ray diffraction (XRD), X-ray photoelectron spectroscopy (XPS), and transmission electron microscopy (TEM), I determined the crystallinity, composition, and microstructure of the pillars. The NbC pillars are substoichiometric, 001-oriented single crystals with B1 structure. I find that the pillars deform plastically with large strains and the compressive yield strength of the pillars increases with decreasing diameter. Throughout this dissertation, any mention of yield strength refers to a compressive yield strength and the values reported here should not be used in the common form of the word that refers to a tensile test. From electron microscopy images, I identify the operation of two slip systems $\{110\}\langle 1\bar{1}0\rangle$ and $\{111\}\langle 1\bar{1}0\rangle$ in

the smaller and relatively larger pillars, respectively, indicating a transition in the slip system based on size. Furthermore, the extended plasticity of the larger pillars is a result of a growing presence of dislocations and their sources with larger pillar sizes. This allows for further plastic deformation with the use of multiple slip systems.

In chapter 4, I present results from *in situ* microcompression tests of VC (001), (110), and (111) pillars at room temperature. The three unique crystal orientations allow for an anisotropic mechanical responses study. I find that each orientation exhibits unique behavior. I find that two orientations of the pillars deform plastically with large strains and the compressive yield strength for all orientations of the pillars increases with decreasing diameter. From the SEM images, I have identified the operation of up to three slip systems dependent on the crystal orientation. The VC(001) pillars are the most plastic and I observed a transition in slip system based on pillar diameter. The VC(110) pillars are described as relatively the hardest because they do not exhibit plastic deformation and are described as brittle. The VC(111) pillars can sustain plastic deformation, however to a lesser extent than VC(001). The mechanical behavior of VC(111) is described as a combination of both VC(001) and VC(110) crystal orientations, mainly hard and with the ability to plastically deform. From the SEM images, I have identified the operation of up to three slip systems dependent on the crystal orientation. The large plasticity in VC crystals at room-temperature is a direct consequence of the simultaneous presence of multiple slip systems within the respective orientation.

In chapter 5, I present results from *in situ* microcompression tests of TaC (110) and (111) pillars at room temperature. The two unique crystal orientations allow for an anisotropic mechanical responses study. I find that each orientation exhibits unique behavior. I find that the pillars deform plastically with moderate strains and the compressive yield strength of the pillars

increases with decreasing diameter. From the SEM images, I have identified the operation of two slip systems dependent on the crystal orientation and pillar diameter, and also the observation of a transition in slip system for both orientations. At room-temperature, the relatively more brittle TaC(110) is a result of only one active slip system per size while the moderate plasticity in TaC(111) crystals is a direct consequence of the simultaneous presence of two slip systems.

In chapter 6, I explore further the many facets of TMCs and how they influence the mechanical behavior. The topics of chemical bonding, temperature, composition, microstructure, and the slip systems are covered briefly to remind the reader of how important every facet is to the behavior of TMCs making their study complex and interesting. The beauty of their complexity is the ability to engineer each of these facets allowing TMCs to be designed and very attractive for various applications.

References

1. L.E. Toth, *Transition metal carbides and nitrides*. 1971, New York: Academic Press.

2. W.S. Williams, *Transition-metal carbides.* Progress in Solid State Chemistry, 1971. **6**: p. 57-118.

3. H.O. Pierson, *Handbook of Refractory Carbides and Nitrides: Properties, Characteristics, Processing, and Applications*. 1996: William Andrew Publishing/Noyes.

4. Y. Zhong, X. Xia, F. Shi, J. Zhan, J. Tu, and H.J. Fan, *Transition Metal Carbides and Nitrides in Energy Storage and Conversion.* Advanced Science, 2016. **3**(5): p. 1500286.

5. B. Eck, R. Dronskowski, M. Takahashi, and S. Kikkawa, *Theoretical calculations on the structures, electronic and magnetic properties of binary 3d transition metal nitrides.* Journal of Materials Chemistry, 1999. **9**(7): p. 1527-1537.

6. C.D. Gelatt, A.R. Williams, and V.L. Moruzzi, *Theory of bonding of transition metals to nontransition metals.* Physical Review B, 1983. **27**(4): p. 2005-2013.

7. R.H.J. Hannink, D.L. Kohlstedt, and M.J. Murray, *Brittle-Region Slip Systems in the Transition-Metal Carbides.* physica status solidi (a), 1971. **6**(1): p. K25-K28.

8. R.H.J. Hannink, D.L. Kohlstedt, M.J. Murray, and D. Tabor, *Slip system determination in cubic carbides by hardness anisotropy.* Proceedings of the Royal Society of London. A. Mathematical and Physical Sciences, 1972. **326**(1566): p. 409-420.

9. W.S. Williams and R.D. Schaal, *Elastic Deformation, Plastic Flow, and Dislocations in Single Crystals of Titanium Carbide.* Journal of Applied Physics, 1962. **33**(3): p. 955-962.

10. R.J. Stokes, T.L. Johnston, and C.H. Li, Trans. Am. Inst. Mining, Me., Petrol. Engrs., 1960. **218**(655).

11. W.S. Williams, *Brittle-ductile behavior of the transition metal carbides.* Propriétés thermodynamiques, physiques et structurales des derives semimetalliques, 1967: p. 181-189.

12. J.R. Greer and W.D. Nix, *Nanoscale gold pillars strengthened through dislocation starvation.* Physical Review B, 2006. **73**(24): p. 245410.

13. S. Korte and W.J. Clegg, *Discussion of the dependence of the effect of size on the yield stress in hard materials studied by microcompression of MgO.* Philosophical Magazine, 2011. **91**(7-9): p. 1150-1162.

14. E.M. Nadgorny, D.M. Dimiduk, and M.D. Uchic, *Size effects in LiF micron-scale single crystals of low dislocation density.* Journal of Materials Research, 2008. **23**(11): p. 2829-2835.

15. J.R. Greer and J.T.M. De Hosson, *Plasticity in small-sized metallic systems: Intrinsic versus extrinsic size effect.* Progress in Materials Science, 2011. **56**(6): p. 654-724.

16. C. Zhou, I.J. Beyerlein, and R. LeSar, *Plastic deformation mechanisms of fcc single crystals at small scales.* Acta Materialia, 2011. **59**(20): p. 7673-7682.

17. S. Kiani, C. Ratsch, A.M. Minor, J.M. Yang, and S. Kodambaka, *In Situ Transmission Electron Microscopy Observations of Room-Temperature Plasticity in Sub-Micron-Size TaC(100) and TaC(011) Single Crystals.* Scripta Materialia, 2014. **100**.

18. S. Kiani, C. Ratsch, A.M. Minor, S. Kodambaka, and J.M. Yang, *Orientation- and Size-Dependent Room-Temperature Plasticity in ZrC Crystals.* Philosophical Magazine, 2015. **95**: p. 1-13.

CHAPTER 2

Experimental Methods

All of my experiments are carried out using the following bulk single-crystals, all purchased from Applied Physics Technologies: a NbC(001) single crystal (2 mm thick and ~3 mm diameter, single-side polished circular disk) with a nominal composition ~$NbC_{x = 0.94}$; VC(001), VC(110), and VC(111) single-crystals (2 mm thick, 2 mm diameter, single-side polished circular disks) with a nominal composition ~$VC_{x = 0.90}$; and TaC(110) and TaC(111) single-crystals (2 mm thick, 2 mm diameter, single-side polished circular disks) with a nominal composition ~$TaC_{x = 0.87}$ (actual range given is $0.80 < x < 0.93$).

2.1 X-Ray Diffraction

An X-ray diffraction (XRD) 2θ–ω scan is obtained from the bulk crystal using a Bede D1 high-resolution diffractometer following the procedure described in Ref. [1]. The crystal is mounted on a miscut Si(001) wafer to eliminate background signal from the diffractometer stage. The optics of the detector and X-ray are aligned to achieve maximum straight-through intensity. The position and inclination of the sample are calibrated with respect to ω and χ (out-of-plane rotation perpendicular to ω) of the desired TMC single-crystal reflection, which for NbC(001) crystals in my experiments is 002 reflection observed at $2\theta = 40.55^{o}$. 2θ–ω scan for 2θ values between 20^{o} and 100^{o} is acquired with a step size of 0.02^{o} and a dwell time of 1 s. An ω scan was obtained for ω values between 5° and 35°. An ω scan of the NbC 002 reflection spanning 30^{o} is acquired with $2\theta = 40.67^{o}$, a step size of 0.02^{o}, and a dwell time of 1 s.

2.2 X-Ray Photoelectron Spectroscopy

X-Ray Photoelectron Spectroscopy (XPS) data are acquired from the same TMC crystal using Kratos Analytical AXIS Ultra DLD. In order to accurately determine the bulk composition and minimize the contribution to the XPS signal from surface contamination, the crystal surface is etched using 3.8 keV Ar^+ ion-beams (with Ar gas pressure at 4×10^{-5} Pa) rastered across 1.7 × 1.7 mm^2 using an extractor current of 100 μA for 20 min. With these parameters, I estimate an etch rate of ~ 0.02 nm/s (corresponding to a depth of ~24 nm), assuming that the etch rates are comparable to TaC_x thin films [2]. Higher resolution C 1*s* and Nb 3*d* spectra are acquired with a step size of 0.1 eV and dwell time of 1 s per step. For NbC(001), the relative concentrations of Nb and C are determined from the ratios of the high-resolution Nb $3d_{5/2}$ and C 1*s* spectral peak areas, measured using CasaXPS software and defined with a Shirley background type [3], corrected by their respective relative sensitivity factors, 1.752 and 0.278. Similar analysis carried out on ZrC thin film samples were found to be accurate to within 14% [4].

2.3 Scanning Electron Microscopy

Scanning electron microscopy (SEM) characterization of the TMC pillars before, during, and after compression testing is carried out using the FEI Nova 600 NanoLab DualBeam™-SEM/FIB system operated with an accelerating voltage of 10 kV and a working distance of 5 mm.

2.4 Focused Ion-Beam

All of the pillars used in my compression tests described below are prepared *via* focused ion-beam (FIB) milling of the bulk crystals in a FEI Nova 600 NanoLab DualBeam™-SEM/FIB

system using 30 keV Ga^+ in two steps: initial coarse milling is carried out with an ion beam current of 3 nA, followed by finer milling using 30 pA ion beams. This milling procedure yields vertical pillars with wider bases and narrower tops with circular cross-section; the tapering angle is < 5°. Note that there is no correlation between the extent of tapering and the diameter of the pillars. I prepared a minimum of 108 such pillars (total of all TMCs) for testing (excluding practice and defective pillars) with initial lengths l_o between 0.9 and 2.2 μm and up to six different sets of top diameters D approximately 0.25, 0.35, 0.45, 0.50, 0.60, and 0.75 μm with average aspect ratios between 2-5 depending on group size.

2.5 Cross-sectional Transmission Electron Microscopy

Cross-sectional transmission electron microscopy (XTEM) characterization is carried out on electron-transparent specimens prepared via focused ion-beam (FIB) milling of compressed pillars using 30 keV Ga^+ ions in an FEI Nova 600 NanoLab DualBeam^{TM}-SEM/FIB system. Prior to milling, the pillar is protected by electron-beam-assisted deposition of ~2 μm thick layer of platinum (Pt) from trimethyl platinum ($C_9H_{16}Pt$) using 30 kV and 0.1 nA. XTEM images of the pillar cross-sections are acquired in a FEI Titan 80-300 kV scanning TEM (S/TEM) operated at 300 kV.

2.6 Microcompression

The microcompression tests are carried out *in situ* in the FEI Nova 600 NanoLab DualBeam^{TM}-SEM/FIB dual system using a Hysitron PI-85 PicoIndenter with a flat-end, 5-μm-wide diamond punch. Each of the pillars is uniaxially compressed at a constant rate of displacement of 1 nm/s. Out of the total amount of TMC pillars, I found that a minimum of five pillars buckled, see for example Figure 2.1. I suspect that the buckling among these pillars,

which were all prepared *via* FIB milling in the same session, is likely due to uneven milling at the base of the pillars and/or slight variation in the tilt of the pillar, which resulted in misalignment of the pillars with respect to the punch. Here, I present only data obtained from the compression of a total of 108 pillars for VC, NbC, and TaC, none of which exhibited noticeable buckling [5]. During each test, load vs. displacement δ data and video-rate (4 frames/s) secondary-electron SEM images are acquired simultaneously with the SEM operated at an accelerating voltage of 10 kV. The resolution in these *in situ* SEM images is ~2.2 nm/pixel. The duration of the compression is limited based on the mechanical response of each pillar. In those pillars exhibiting large displacement bursts (relative macroscale shear) that can potentially result in complete fracture, the test is immediately ended following the shear event to preserve the pillar for imaging its post-compression morphology and the determination of slip plane(s). In case the pillar undergoes plastic deformation via multiple smaller-scale slip events instead of large strain bursts, then the compression is continued until the larger displacement event. In these experiments, the extent of all of the individual displacements δ vary and the range encompassing all of the pillar displacements is approximately 50 nm to 610 nm.

2.7 Post-compression Scanning Electron Microscopy

Higher-resolution scanning electron microscopy (HRSEM) images of the pillars are acquired after the compression tests using Through the Lens Detector in the same FEI Nova 600 NanoLab DualBeam^{TM}-SEM/FIB dual system operated at 10 kV. From the SEM images, using the SEM software, I measure D, orientations ϕ' [= (90-ϕ)] of the slip bands with respect to the pillar axes, and the pillar lengths, l_0 and l_f, before and after the compression tests, respectively. The angles ϕ' are measured after the SEM images are tilt-corrected for cross-section using the

SEM software. (I define ϕ as the angle between normal to the slip band and the pillar axis.) To avoid potential artefacts associated with measuring orientations of tilted slip traces from SEM images of cylindrical pillars, I acquired images of the pillars at several different rotations. Here, I present only those SEM images, in which slip traces appear normal to the viewer. Based on my measurements, the angles ϕ reported here are accurate to within 2°. All pillars have measurement uncertainties associated with the D values that can vary between 5 and 40 nm, depending on the pillar, as a result of which errors in applied stresses σ ($\propto 1/D^2$) can be between 0.6 and 17.4%. Note that the tip displacement δ, as recorded by the indenter software, may differ from the actual deformation induced changes in the lengths of the pillar. In my experiments, I find that the accuracy in δ values is inversely proportional to the duration of the test. Therefore, to minimize the errors in determination of plastic strain $\varepsilon_p = (l_0 - l_f)/l_0$, I rely on direct measurements of both l_0 and l_f of a given pillar from SEM images acquired before and after the compression test. I realize that accurate determination of the pillar lengths (l_0 and l_f) is not straightforward because bases of the pillars are not well-defined due to variations in depths caused by the FIB milling around the pillars. To minimize the uncertainties in pillar lengths, I measure both l_0 and l_f from the *same* arbitrarily chosen reference point near the base to the pillar top before and after compression, respectively. With this approach, the decrease in pillar length ($l_0 - l_f$) due to compression is accurate to within ± 5 nm, irrespective of the uncertainties in l_0 and l_f and the errors in ε_p are < 3%. Note that these errors are considerably larger than what can be accounted for using, for example, Sneddon's correction [6].

2.8 Yield Strength Calculation

Yield strengths, σ_y, are determined from the $\sigma(\delta)$ curves as follows: first, I choose portions of the σ vs. δ data that are well within the linear elastic and nonlinear plastic regions. (In the linear elastic regime, I limit my analysis to $\sigma > 2$ GPa and discard the spurious non-linear variations in δ observed at lower σ (≤ 2 GPa) values caused by inhomogeneities at the tip-pillar contact interfaces during the early stages of loading.) Next, the two sets of σ vs. δ data, plotted on a logarithmic scale, are fit using linear least-squares analysis. The linear fits are extended such that they intersect, and the point of intersection is defined as σ_y. (An alternate approach to determining σ_y involves use of a plastic strain offset to make the lines intersect. This approach results in slightly higher σ_y values but the observed trend in $\sigma_y(D)$ will be the same.) The errors in σ_y values are determined by varying the ranges of the elastic and plastic portions of the σ vs. δ data and are $\pm$ 0.4 GPa.

2.9 Figures

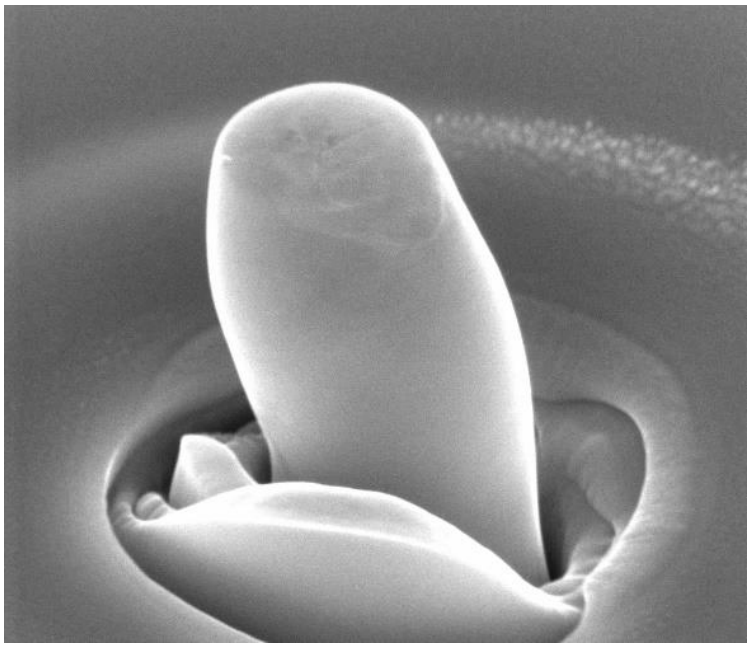

Figure 2.1: Example of buckling observed for a NbC(001) pillar. The bending of this pillar is a good example of plasticity in NbC. The pillar could have continued to deform further, however, the compression test was ended to preserve the pillar and document the observation.

References

1. A. Aleman, C. Li, H. Zaid, H. Kindlund, J. Fankhauser, S.V. Prikhodko, M.S. Goorsky, and S. Kodambaka, *Ultra-high vacuum dc magnetron sputter-deposition of epitaxial Pd(111)/Al2O3(0001) thin films.* Journal of Vacuum Science & Technology A, 2018. **36**(3).

2. K. Tanaka, A. Aleman, M. Liao, Y. Wang, M. Goorsky, and S. Kodambaka, *Effects of ultra-low ethylene partial pressure on microstructure and composition of reactively sputter-deposited Ta–C thin films.* Thin Solid Films, 2019. **688**: p. 137440.

3. D.A. Shirley, *High-Resolution X-Ray Photoemission Spectrum of the Valence Bands of Gold.* Physical Review B, 1972. **5**: p. 4709-4714.

4. H. Zaid, A. Aleman, K. Tanaka, C. Li, P. Berger, T. Back, J. Fankhauser, M.S. Goorsky, and S. Kodambaka, *Influence of ultra-low ethylene partial pressure on microstructural and compositional evolution of sputter-deposited Zr-C thin films.* Surface and Coatings Technology, 2020. **398**: p. 126053.

5. H. Zaid, K. Tanaka, C.V. Ciobanu, J.-M. Yang, S. Kodambaka, and H. Kindlund, *Growth of elastically-stiff, nanostructured, high-entropy alloy nitride, (VNbTaMoW)N/Al2O3(0001) thin film.* Scripta Materialia, 2021. **197**: p. 113813.

6. H. Fei, A. Abraham, N. Chawla, and H. Jiang, *Evaluation of Micro-Pillar Compression Tests for Accurate Determination of Elastic-Plastic Constitutive Relations.* Journal of Applied Mechanics, 2012. **79**(6).

CHAPTER 3

Size-dependent Mechanical Responses in NbC(001) Single-Crystals

3.1 Introduction

Among the group 5 TMCs, niobium carbide (NbC) is a hard (~22 GPa), high Young's modulus (E ~510 GPa), and high melting point (T_m = 3873 K) solid with good electrical conductivity (~3 × 10^6 Ω^{-1} m^{-1} at 300 K) and Hall coefficient (-1.3 × 10^{-10} m^3/K) [1]. Microindentation tests [2-4] carried out at room-temperature on bulk 001-oriented NbC_x single-crystals with $0.75 \leq x \leq 1$ revealed hardness anisotropy and the operation of two slip systems, $\{110\}\langle 1\bar{1}0\rangle$ + $\{111\}\langle 1\bar{1}0\rangle$, at room-temperature [2]. Four point bending tests conducted on bulk polycrystalline NbC samples revealed ductile-brittle transition at 1750 K [5]. However, there are no reports on mechanical responses of NbC subjected to uniaxial loading at room-temperature. Here, as a first step, I focus on uniaxial compression of 001-oriented NbC single-crystals at room-temperature. To avoid potential influence of extrinsic factors such as voids and cracks on the mechanical behavior of bulk NbC crystals, I use carefully prepared sub-micrometer size pillars. Micro-compression tests [6] conducted on non-metallic materials that are generally considered to be brittle have provided valuable insights into the influence of size on plasticity [7-16]. Among the TMCs, previous studies have shown that small-scale single-crystals of ZrC and TaC can undergo plastic deformation under compression [17].

In this chapter, I present results obtained from X-ray diffraction (XRD), X-ray photoelectron spectroscopy (XPS), and microcompression of a commercially available NbC(001) single-crystal. I determined that the bulk sample is nearly stoichiometric and B1-structured NbC(001) single-crystal. Compression of sub-micrometer-scale NbC(001) pillars reveal

considerable plasticity, strain hardening, and size-dependent yield strengths. From electron microscopy characterization of the deformed pillars, I identify $\{110\}\langle 1\bar{1}0\rangle$ and $\{111\}\langle 1\bar{1}0\rangle$ as the two active slip systems in these small-scale pillars.

3.2 Results

Figure 3.1(a) is an XRD 2θ-ω scan obtained from the bulk NbC(001) sample. I find two peaks at 2θ = 40.55 ± 0.02° and 87.52 ± 0.02°, identified as the 002 and 004 reflections, respectively, of B1-NbC. From these peaks, expected of a 001-oriented single-crystal, I measure a lattice constant of 0.4446 ± 0.0002 nm, ~ 0.6% smaller than the reported value for stoichiometric NbC bulk[1, 18]. Inset in Figure 3.1(a) shows an ω scan of the 002 reflection with a full width at half maximum Γ of 0.04 ± 0.02°, indicative of a high-quality crystal. Based on C-concentration dependent variations in NbC_x lattice parameters [18], the measured lattice parameter corresponds to substoichiometric NbC_x with $x = 0.78$.

The composition of the NbC bulk is also quantified by XPS. Figure 3.1(b) shows high resolution XPS data around C 1*s* and Nb 3*d* peaks from the NbC(001) sputter-etched surface, represented by red and green circles, respectively. Within the C 1*s* spectrum, I identify at least two peaks, one associated with C-Nb bonds (at ~282.8 eV) and the other characteristic of C-C bonds [19], shown using blue and black curves, respectively. (The C-C peak is in principle a convolution of peaks due to sp^2 and/or sp^3 bonded carbon, expected at ~284.3 and ~284.7 eV, respectively [20].) The peaks observed at binding energies between 201 and 211 eV correspond to Nb $3d_{5/2}$ and Nb $3d_{3/2}$, respectively. From the areas of the C-C, Nb $3d_{5/2}$ and C-Nb peaks and assuming that the C-C peak is solely due to free-carbon, the determined bonded C content, $x = 0.99$, i.e. $NbC_{0.99}$. However, the depth-dependent XPS data (not shown here) reveal that the

amount of free C with respect to the total C content decreases from ~47 at.% to < 7 at.% with increasing etching time from 5 to 20 min. This discrepancy in C-content values could arise due to rather large uncertainty (up to 14 at.%) associated with the XPS quantification procedure [21].

In the following section, I first focus on mechanical responses of FIB-milled pillars subjected to uniaxial compression *in situ* in the SEM. Fig. 3.2 shows representative SEM images acquired from the bulk NbC(001) single-crystal with pillars of top diameters D = (a) 0.24 μm, (b) 0.46 μm, and (c) 0.76 μm (top panel) before and (bottom panel) after compression. For each of the pillars, lengths l_o and l_f, before and after compression, are shown using white arrows. Clearly, lengths of all the three pillars decreased, while their average diameters increased upon compression, i.e. the pillars deformed plastically. This behavior is typical of four out of five pillars with $D \approx 0.25$ μm and $D \approx 0.50$ μm and all eight pillars with $D \approx 0.75$ μm. The other two pillars fractured without significant deformation. (Note that buckling observed in Figure 2.1 is also indicative of plasticity.) For those unfractured pillars, I estimate plastic strains ε_p between 2 and 6% for $D \sim 0.25$ μm, 3 and 10% for $D \sim 0.50$ μm, and 2 and 30% for $D \sim 0.75$ μm. (see, for example, Figure 3.2.

Engineering stress σ vs. displacement δ data obtained during the *in situ* compression of all the 18 pillars are plotted in Figures 3.2(d), (e), and (f) for pillars with D around 0.25 μm, 0.50 μm, and 0.75 μm, respectively. The $\sigma(\delta)$ data corresponding to the pillars in Figures 3.2(a)-(c) are highlighted using red, green, and blue colors, respectively. During the initial stages of loading, I observed a linear elastic behavior; δ increases linearly with increasing σ up to the yield point σ_y, followed by a smooth transition to non-linear plastic deformation. At $\sigma > \sigma_y$, I observe two interesting phenomena: 1) sudden drops in σ, due to displacement bursts, whose amplitude appears to increase with decreasing D and 2) the rate of strain hardening appears to be higher in

pillars with smaller D ($\approx$ 0.25 μm) than in those with $D \gtrsim$ 0.5 μm. Similar size-dependent displacement bursts have been observed in single- and poly-crystals [22-26]; and size-dependent strain hardening rates have been observed in single-crystalline face-centered cubic Cu [27, 28] and single-crystalline body-centered cubic Mo, Ta, Nb, and W [29] pillars and attributed to size-dependent dislocation dynamics [28], and dislocation avalanches [24].

Yield strengths σ_y of all 18 pillars are extracted from the σ vs δ curves in Figures 3.2(d-f) and plotted as a function of D in Figure 3.3(a). I find that σ_y increases as D decreases, from 9.7 ± 0.7 GPa for pillars with $D \approx$ 0.75 μm to 17 ± 2 GPa for pillars with $D \approx$ 0.25 μm.

To gain insights into the observed phenomena of size-dependent plastic deformation, I carried out post-compression electron microscopy investigation of the compressed pillars. Figures 3.4(a)-(c) are typical higher resolution SEM images obtained after compression of three pillars with $D \approx$ (a) 0.24 μm, (b) 0.46 μm, and (c) 0.76 μm. In Figures 3.4(a) and (b), I observed localized deformation in the form of a slip band from the top surface and leading across the body of the pillars. In case of larger size pillars with $D \approx$ 0.75 μm, I did not find any such slip bands in the SEM image [Figure 3.4(c)], presumably due to deformation via continuous slip with smaller displacement amplitudes as seen in Figure 3.2(d). I noted that among all the pillars I have tested, two of the pillars with $D \leq$ 0.50 μm show clear evidence of slip but I have not identified slip traces in the larger size pillars (i.e., $D \approx$ 0.75 μm). In the smaller pillar [Figure 3.4(a)], I found that the shear band is oriented at $\phi' \approx 45°$, i.e. $\phi \approx 45°$. Since the pillar axis is [001], the possible slip planes that are oriented at 45° with respect to the pillar axis belong to {110}. Based on this result, I concluded that the operating slip system in this pillar is $\{110\}\langle 1\bar{1}0\rangle$. In the intermediate size pillar with $D \approx$ 0.46 μm [Figure 3.4(b)], I found that the slip trace is $\phi' \approx 54°$ with respect to

the pillar axis, i.e. $\phi \approx 36°$, which I argue (and provide justification below) that is not a $\{110\}\langle 1\bar{1}0\rangle$ slip system.

Figure 3.4(d) is a typical TEM image acquired from a FIB-milled electron-transparent cross-section of the compressed pillar with $D \approx 0.46$ μm, shown in Figure 3.4(b). Inset in Figure 3.4(d) is a selected area electron diffraction (SAED) pattern obtained from the same field of view with zone axis [001]. Note that both the TEM image and the SAED in Figure 3.4(d) are obtained using the *same* sample/beam tilt. NbC {200} and {220} reflections are highlighted using yellow and red circles, respectively. The observed 4-fold symmetry of the diffraction spots and the absence of any other reflections indicate that the compressed pillar remains single-crystalline with B1 structure. That is, I do not observe any deformation induced lattice distortions, phase transformation, and/or twinning in the pillars. I therefore do not expect any deviations in the orientations of the crystal planes measured from the images. I found slip traces in the images, which appear as darker contrast parallel sets of lines. Dashed and dotted green lines in Figures 3.4(d) are drawn perpendicular to the visible slip traces. The [001] axis of the pillar is highlighted in the TEM images using solid yellow lines, drawn perpendicular to a dotted yellow line passing through the central (000) spot and {200} diffraction spots in the SAED (see Figure 4(d) inset). The dotted green line passing through the (000) spot in the SAED does not intersect {220} spots, i.e. the observed slip traces do not correspond to {110} planes. I measure $\phi_1 = 56 \pm 2°$ and $\phi_2 = 50 \pm 2°$ as the angles between the normals to the slip traces and the [001] pillar axis (see Figure 3.4d). In comparison, the angles between normal vectors of the (111) and (011) slip planes and [001] pillar axis, are 54.7° and 45°, respectively.

I found that ϕ_1 is, within the measurement uncertainties of 2°, comparable to 54.7°, i.e. the slip traces visible in Figure 3.4(d) are likely due to {111} slip planes. I attribute the visibility of {111} slip traces in the TEM image to thin cross-sectional specimen and possibly some misorientation/bending of the FIB-prepared sample during imaging. However, given that ϕ_2 is within 5° of both 45° and 54.7°, I cannot unequivocally confirm the crystallographic orientation of the observed slip traces solely from the ϕ_2 measurement. (While imaging with [011] zone axis is ideal for visualizing {111} planes, it was not possible to tilt the TEM sample to the desired angle.) In order to determine the orientation of the slip planes associated with ϕ_2, I rely on the interplanar angle θ, which I measure as 76 ± 2°; this value is comparable to 70.5°, the angle between any two non-parallel {111} planes and considerably different from 35.3° and 90°, the two possible angles between {111} and {110} planes. Based on these measurements, I conclude that the slip traces observed in the TEM images are due to {111} planes, consistent with my interpretation of the slip trace angles measured from SEM image in Figure 3.4(b). With the assumption that $\langle 1\bar{1}0 \rangle$ is the slip direction, generally expected in B1 crystals, these results indicate the operation of $\{111\}\langle 1\bar{1}0 \rangle$ slip system.

3.3 Discussion

While the operation of both $\{110\}\langle 1\bar{1}0 \rangle$ and $\{111\}\langle 1\bar{1}0 \rangle$ slip systems have been observed during microindentation of bulk NbC(001) and other group 5 TMC(001) single-crystals at room-temperature [2], there are no reports of the activation of two slip systems during room-temperature compression of 001-oriented group 5 TMC crystals. (Previous reports identified $\{110\}\langle 1\bar{1}0 \rangle$ as the only slip system during uniaxial compression of 001-oriented single-crystalline TaC pillars with D < 0.5 μm [30]; in 110-oriented Ta-C-N pillars, $\{111\}\langle 1\bar{1}0 \rangle$ is

found to be the only active slip system [31]. I speculate that the observed differences between the two group 5 TMCs may be due to differences in pillar sizes, C-contents, and loading rates.

Microcompression tests conducted on NbC(001) single-crystal reveal variations in σ_y with D, phenomena well-documented in the literature [26]. What I find surprising, however, is the extent of plastic strain ε_p observed during compression of NbC(001) pillars that is considerably higher than the strains reported in other B1-structured 001-oriented TMCs such as TaC(100) and ZrC(100) single-crystals subjected to similar microcompression tests [30, 32].

To consistently explain all of my observations -- size-dependent yield strengths, strain hardening, displacement burst amplitudes, extensive plastic strain, and the operation of multiple slip systems -- I propose that number of dislocations (or dislocation sources) scales with pillar size and assume that dislocation mobility is facile along $\{111\}\langle 1\bar{1}0\rangle$ slip system compared to $\{110\}\langle 1\bar{1}0\rangle$. In smaller size pillars (e.g., D ~0.25 μm), number of dislocations (and sources) within the bulk of the crystal is expected to be low and plastic deformation is likely to be controlled by the surface nucleation of dislocations [33] along energetically the most favorable slip system (i.e., $\{110\}\langle 1\bar{1}0\rangle$) [30, 32]. Consequently, slip events are expected to be finite and discontinuous resulting in displacement bursts with larger amplitudes and higher yield strength. With increasing pillar size, both surface nucleation and multiplication of internal dislocations lead to higher number of dislocations and the activation of $\{111\}\langle 1\bar{1}0\rangle$ slip system, which results in more continuous slip with smaller amplitude displacement bursts, larger plastic strain, and lower yield strength. Inherent in my model is the speculation that the $\{110\}\langle 1\bar{1}0\rangle$ and $\{111\}\langle 1\bar{1}0\rangle$ slip systems are dominant in smaller and large-size crystals, respectively. Based on this model, using $\sigma_y \approx 17$ GPa for small D and 9.7 GPa for large D pillars and with Schmid factors β_{110} =

0.50 for $\{110\}\langle 1\bar{1}0\rangle$ and $\beta_{111} \approx 0.41$ for $\{111\}\langle 1\bar{1}0\rangle$ slip systems, I estimate critical resolved shear stresses of ≈ 8.5 GPa for $\{110\}\langle 1\bar{1}0\rangle$ and ≈ 4 GPa for $\{111\}\langle 1\bar{1}0\rangle$ slip systems. Furthermore, the operation of two slip systems $\{110\}\langle 1\bar{1}0\rangle$ and $\{111\}\langle 1\bar{1}0\rangle$ in the smaller and relatively larger pillars, respectively, indicate a transition in the slip system based on size. Clearly, additional microcompression data from pillars of additional sizes within the sub-micrometer range and TEM characterization of the slip bands are needed to verify size-dependent activation of a specific slip system and to identify the likely existence of a transitional size, where both slip systems can be active.

3.4 Conclusion

In summary, I determined the crystallinity, composition, and micromechanical responses of a commercially available bulk NbC(001) single-crystal. From X-ray photoelectron spectroscopy and X-ray diffraction measurements, I measure Nb/C ratio as ~1.01 and B1 lattice parameter as 0.4446 ± 0.0002 nm. *In situ* SEM based compression of cylindrical NbC(001) pillars with sub-micrometer size diameters revealed that the pillars deform plastically with large strains and diameter-dependent yield strengths that increase with decreasing diameter. From electron microscopy images, I identify the operation of two slip systems, $\{110\}\langle 1\bar{1}0\rangle$ and $\{111\}\langle 1\bar{1}0\rangle$. Based on my results, I suggest that the unexpectedly large plasticity in NbC(001) crystals at room-temperature is a direct consequence of the easy slip along $\{111\}\langle 1\bar{1}0\rangle$. My results also point to the exciting possibility of designing bulk refractory TMCs with superior plasticity by optimizing the grain sizes, orientations, and composition that promotes the activation of desired slip systems.

3.5 Figures

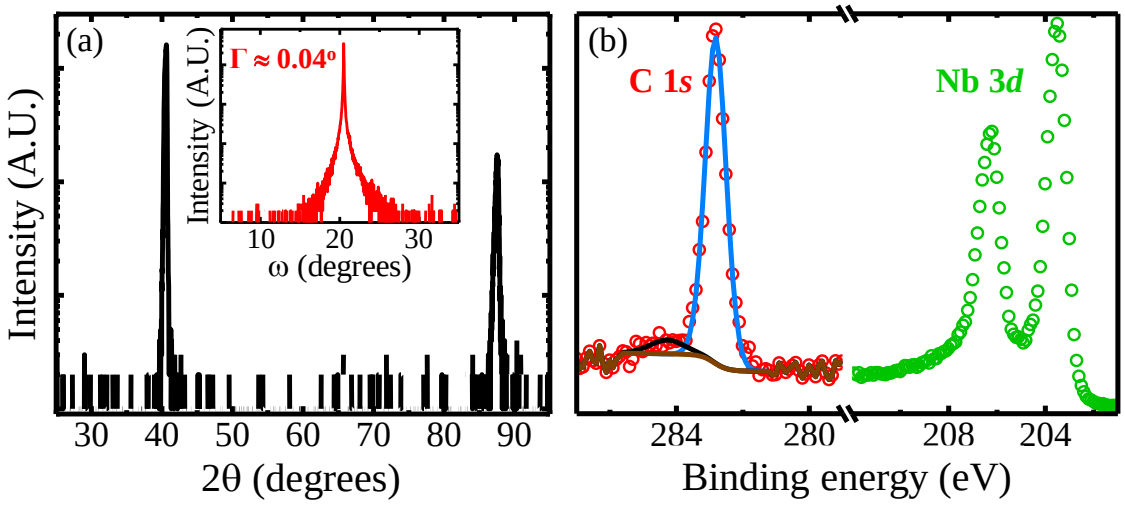

Figure 3.1: (a) X-ray diffraction (XRD) ω-2θ scan obtained from a bulk NbC(001) single-crystal. Inset shows an ω scan of the 002 reflection and measure the full width at half maximum $\Gamma = 0.04 \pm 0.02^{o}$. (b) High resolution X-ray photoelectron spectra (XPS) acquired around C 1*s* (red circles) and Nb 3*d* peaks (green circles) from the same bulk sample. The green, blue, and black curves represent Nb 3*d* peaks, C-Nb, and C-C components, respectively. The brown curve denotes the background signal in the spectra.

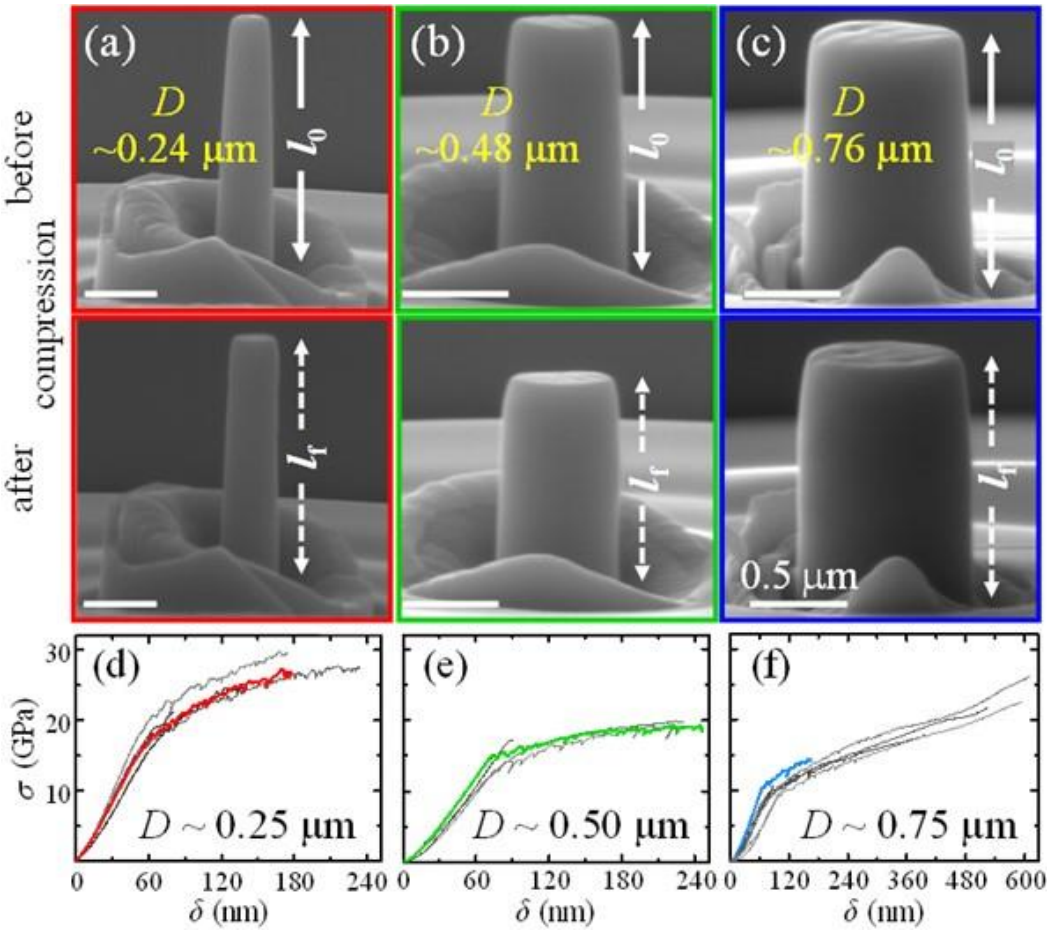

Figure 3.2: (a-c) Representative SEM images acquired from the bulk NbC(001) with pillars of top diameters D = a) 0.24, b) 0.48, and c) 0.76 μm before (top panel) and after compression (bottom panel). In the images, l_o and l_f refer to lengths of the pillars before and after compression, respectively, measured from the top with respect to the same arbitrarily chosen reference points near the bases of the pillars. (d-f) Plots of engineering stress (σ) vs. displacement (δ) data obtained during *in situ* compression of three sets of pillars with D around (d) 0.25, (e) 0.50, and (f) 0.75 μm. The $\sigma(\delta)$ data corresponding to the pillars in (a), (b), and (c) are shown using red, green, and blue curves, respectively.

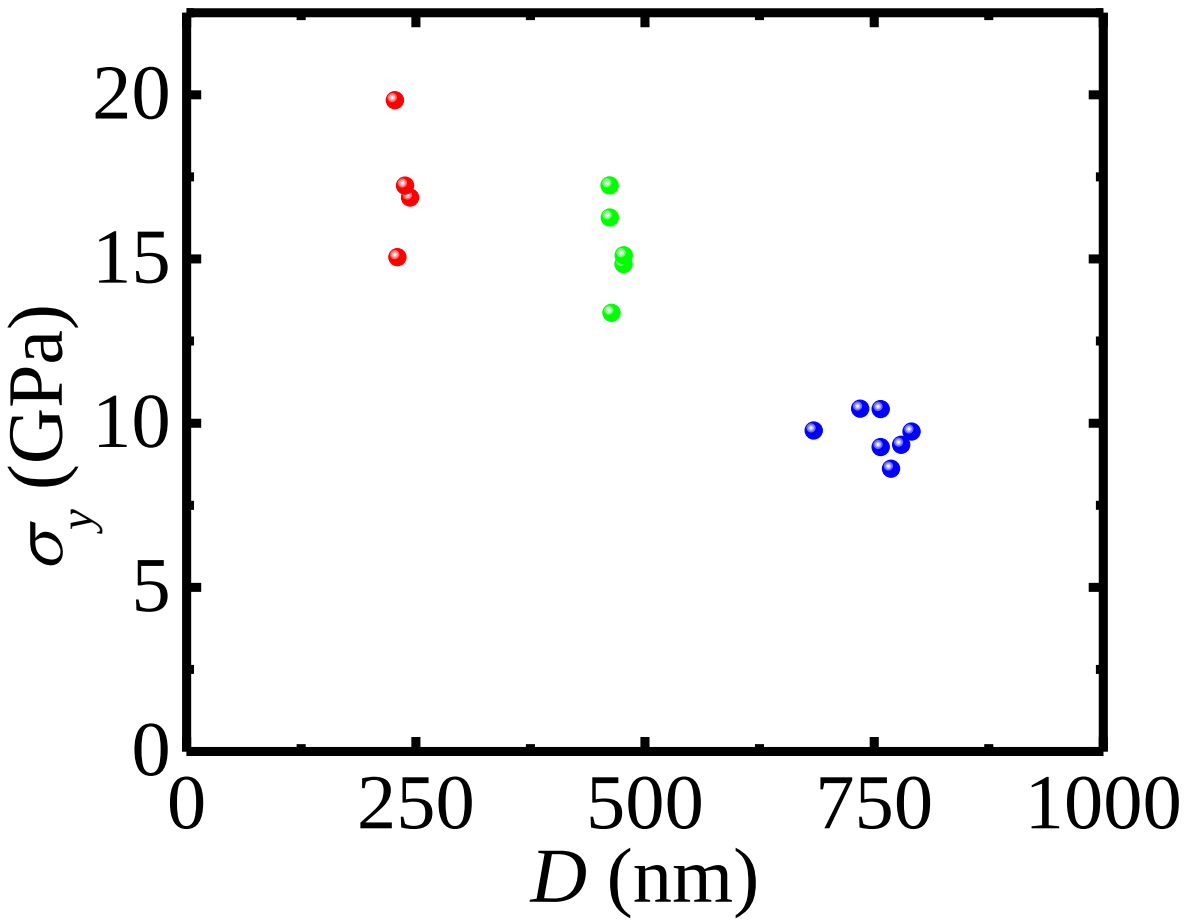

Figure 3.3: Plot of yield strength σ_y vs. D, extracted from compression tests of 18 pillars from Figure 3.2.

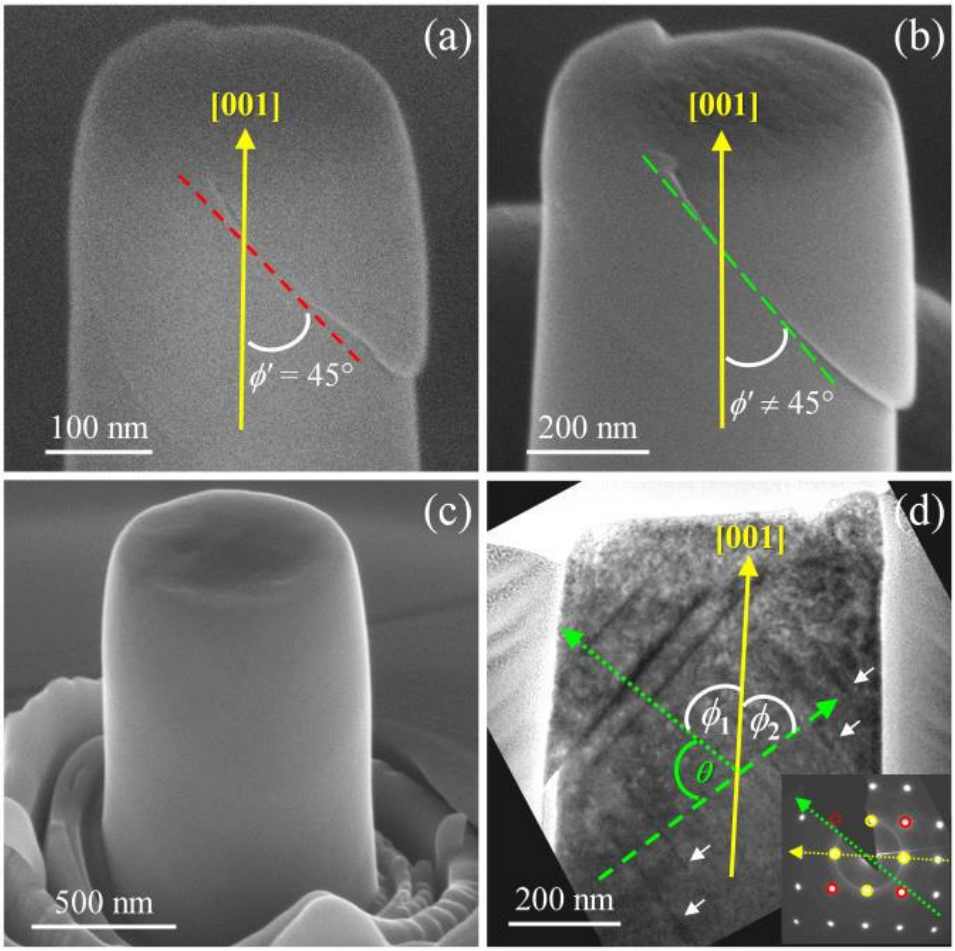

Figure 3.4: (a-c) Typical SEM images (60°-tilt) acquired after the compression of three different NbC(001) pillars with $D \approx$ (a) 0.24 μm, (b) 0.46 μm, and (c) 0.76 μm. Dashed red and green lines, respectively, in (a) and (b) highlight the orientations ϕ' [= (90-ϕ)] of the slip bands with respect to the [001] pillar axes, where ϕ is the angle between normal to the slip trace and the pillar axis. (d) Representative bright field transmission electron microscopy (TEM) image obtained from an electron-transparent cross-section of the compressed pillar shown here in (b). Associated selected area electron diffraction (SAED) pattern with zone axis [001] of the same area of the pillar is shown as inset. Yellow and red circles indicate NbC {200} and {220} reflections, respectively. Solid yellow line denotes pillar axis and is drawn perpendicular to a dotted yellow line passing through the central (000) spot and {200} diffraction spots in the SAED. Dashed and dotted green lines are drawn perpendicular to darker contrast parallel sets of lines highlighted by white arrows, which I identify as slip traces. The angles, $\phi_1 = 56 \pm 2°$, $\phi_2 = 50 \pm 2°$, are measured between normals to the slip traces and the pillar axis and $\theta = 76 \pm 2°$ is the angle between the two sets of slip traces based on which I conclude that {111} are the slip planes.

References

1. L.E. Toth, *Transition metal carbides and nitrides*. 1971, New York: Academic Press.

2. R.H.J. Hannink, D.L. Kohlstedt, M.J. Murray, and D. Tabor, *Slip system determination in cubic carbides by hardness anisotropy.* Proceedings of the Royal Society of London. A. Mathematical and Physical Sciences, 1972. **326**(1566): p. 409-420.

3. G. Morgan and M.H. Lewis, *Hardness anisotropy in niobium carbide.* Journal of Materials Science, 1974. **9**(3): p. 349-358.

4. I.L. Shabalin, *Ultra-High Temperature Materials II: Refractory Carbides I (Ta, Hf, Nb and Zr Carbides)*. 2019: Springer Netherlands. 755.

5. A. Kelly and D.J. Rowcliffe, *Deformation of Poly crystalline Transition Metal Carbides.* Journal of the American Ceramic Society, 1967. **50**(5): p. 253-256.

6. D. Kiener, C. Motz, and G. Dehm, *Micro-compression testing: A critical discussion of experimental constraints.* Materials Science and Engineering: A, 2009. **505**(1): p. 79-87.

7. S. Korte and W.J. Clegg, *Discussion of the dependence of the effect of size on the yield stress in hard materials studied by microcompression of MgO.* Philosophical Magazine, 2011. **91**(7-9): p. 1150-1162.

8. R. Soler, J.M. Wheeler, H.-J. Chang, J. Segurado, J. Michler, J. Llorca, and J.M. Molina-Aldareguia, *Understanding size effects on the strength of single crystals through high-temperature micropillar compression.* Acta Materialia, 2014. **81**: p. 50-57.

9. J.M. Wheeler, C. Niederberger, C. Tessarek, S. Christiansen, and J. Michler, *Extraction of plasticity parameters of GaN with high temperature, in situ micro-compression.* International Journal of Plasticity, 2013. **40**: p. 140-151.

10. P.R. Howie, S. Korte, and W.J. Clegg, *Fracture modes in micropillar compression of brittle crystals.* Journal of Materials Research, 2012. **27**(1): p. 141-151.

11. F. Östlund, P.R. Howie, R. Ghisleni, S. Korte, K. Leifer, W.J. Clegg, and J. Michler, *Ductile–brittle transition in micropillar compression of GaAs at room temperature.* Philosophical Magazine, 2011. **91**(7-9): p. 1190-1199.

12. F. Östlund, K. Rzepiejewska-Malyska, K. Leifer, L.M. Hale, Y. Tang, R. Ballarini, W.W. Gerberich, and J. Michler, *Brittle-to-Ductile Transition in Uniaxial Compression of Silicon Pillars at Room Temperature.* Advanced Functional Materials, 2009. **19**(15): p. 2439-2444.

13. W.W. Gerberich, J. Michler, W.M. Mook, R. Ghisleni, F. Östlund, D.D. Stauffer, and R. Ballarini, *Scale effects for strength, ductility, and toughness in "brittle" materials.* Journal of Materials Research, 2009. **24**(3): p. 898-906.

14. D. Jang and J.R. Greer, *Transition from a strong-yet-brittle to a stronger-and-ductile state by size reduction of metallic glasses.* Nature Materials, 2010. **9**(3): p. 215-219.

15. Z.W. Shan, J. Li, Y.Q. Cheng, A.M. Minor, S.A. Syed Asif, O.L. Warren, and E. Ma, *Plastic flow and failure resistance of metallic glass: Insight from in situ compression of nanopillars.* Physical Review B, 2008. **77**(15): p. 155419.

16. S. Kiani, K.W.K. Leung, V. Radmilovic, A.M. Minor, J.M. Yang, D.H. Warner, and S. Kodambaka, *Dislocation glide-controlled room-temperature plasticity in 6H-SiC single crystals.* Acta Materialia, 2014. **80**: p. 400-406.

17. S. Kiani, J.-M. Yang, and S. Kodambaka, *Nanomechanics of Refractory Transition-Metal Carbides: A Path to Discovering Plasticity in Hard Ceramics.* Journal of the American Ceramic Society, 2015. **98**(8): p. 2313-2323.

18. M.G.D.V. Cuppari and S.F. Santos, *Physical Properties of the NbC Carbide.* Metals, 2016. **6**(10): p. 250.

19. A. Gupta, M. Mittal, M.K. Singh, S.L. Suib, and O.P. Pandey, *Low temperature synthesis of NbC/C nano-composites as visible light photoactive catalyst.* Scientific reports, 2018. **8**(1): p. 13597.

20. R. Blume, D. Rosenthal, J.-P. Tessonnier, H. Li, A. Knop-Gericke, and R. Schlögl, *Characterizing Graphitic Carbon with X-ray Photoelectron Spectroscopy: A Step-by-Step Approach.* ChemCatChem, 2015. **7**(18): p. 2871-2881.

21. H. Zaid, A. Aleman, K. Tanaka, C. Li, P. Berger, T. Back, J. Fankhauser, M.S. Goorsky, and S. Kodambaka, *Influence of ultra-low ethylene partial pressure on microstructural and compositional evolution of sputter-deposited Zr-C thin films.* Surface and Coatings Technology, 2020. **398**: p. 126053.

22. M.D. Uchic, P.A. Shade, and D.M. Dimiduk, *Plasticity of Micrometer-Scale Single Crystals in Compression.* Annual Review of Materials Research, 2009. **39**(1): p. 361-386.

23. S. Papanikolaou, Y. Cui, and N. Ghoniem, *Avalanches and plastic flow in crystal plasticity: an overview.* Modelling and Simulation in Materials Science and Engineering, 2017. **26**(1): p. 013001.

24. F.F. Csikor, C. Motz, D. Weygand, M. Zaiser, and S. Zapperi, *Dislocation Avalanches, Strain Bursts, and the Problem of Plastic Forming at the Micrometer Scale.* Science, 2007. **318**(5848): p. 251-254.

25. H. Zaid, A. Aleman, and S. Kodambaka, *Size-dependent yielding and strain-hardening of compositionally-enriched body-centered cubic VNbTaMoW alloy.* Scripta Materialia, 2020. **178**: p. 518-521.

26. J.R. Greer and J.T.M. De Hosson, *Plasticity in small-sized metallic systems: Intrinsic versus extrinsic size effect.* Progress in Materials Science, 2011. **56**(6): p. 654-724.

27. J.M. Wheeler, C. Kirchlechner, J.-S. Micha, J. Michler, and D. Kiener, *The effect of size on the strength of FCC metals at elevated temperatures: annealed copper.* Philosophical Magazine, 2016. **96**(32-34): p. 3379-3395.

28. D. Kiener, P.J. Guruprasad, S.M. Keralavarma, G. Dehm, and A.A. Benzerga, *Work hardening in micropillar compression: In situ experiments and modeling.* Acta Materialia, 2011. **59**(10): p. 3825-3840.

29. A.S. Schneider, D. Kaufmann, B.G. Clark, C.P. Frick, P.A. Gruber, R. Mönig, O. Kraft, and E. Arzt, *Correlation between Critical Temperature and Strength of Small-Scale bcc Pillars.* Physical Review Letters, 2009. **103**(10): p. 105501.

30. S. Kiani, C. Ratsch, A.M. Minor, J.M. Yang, and S. Kodambaka, *In Situ Transmission Electron Microscopy Observations of Room-Temperature Plasticity in Sub-Micron-Size TaC(100) and TaC(011) Single Crystals.* Scripta Materialia, 2014. **100**.

31. T. Glechner, R. Hahn, T. Wojcik, D. Holec, S. Kolozsvári, H. Zaid, S. Kodambaka, P.H. Mayrhofer, and H. Riedl, *Assessment of ductile character in superhard Ta-C-N thin films.* Acta Materialia, 2019. **179**: p. 17-25.

32. S. Kiani, C. Ratsch, A.M. Minor, S. Kodambaka, and J.M. Yang, *Orientation- and Size-Dependent Room-Temperature Plasticity in ZrC Crystals.* Philosophical Magazine, 2015. **95**: p. 1-13.

33. C. Zhou, I.J. Beyerlein, and R. LeSar, *Plastic deformation mechanisms of fcc single crystals at small scales.* Acta Materialia, 2011. **59**(20): p. 7673-7682.

CHAPTER 4

Anisotropic Mechanical Responses in VC Single-Crystals

4.1 Introduction

Transition metal carbides (TMCs) of group 4 and 5 with B-1 type structure have a mixture of ionic, covalent, and metallic bonds [1-3]. They are considered ultra-high temperature ceramics with some of the highest known melting temperatures (T_m > 2900 K), extremely stiff (elastic moduli > 250 GPa), extremely hard (>10 GPa) with good thermal and electrical conductivities, good thermomechanical and chemical properties that exhibit resistance to wear, ablation, and corrosion [1]. TMCs are used for hard protective coatings [3] and attractive for high-temperature structural components in aerospace and automotive applications [2, 3]. However, given that these materials exhibit superior properties, their low temperature applications have seen limited use because of their inherent bonding and ceramic-like nature. TMCs are generally considered brittle at room-temperature, however, local plasticity under room-temperature microindentation has been reported [4] and for temperatures as low as 77 K [5]. Although TMCs are considered brittle under uniaxial loading or bending at low temperatures, they behave ductile at elevated temperatures (> $0.3T_m$) [1]. While it is generally expected that the primary slip system for B1-structured TMCs is {111}[110] at high temperatures [1], other slip systems can be activated depending on temperature and the transition-metal [6].

Vanadium carbide is among the most commonly used of the cubic transition metal carbides. Its applications include it as an important structural component of alloyed steels widely used in the aircraft and automobile industries, as a grain growth inhibitor in tungsten carbide

based hard metals [3, 7], and as a nanocrystalline vanadium carbide as a catalyst for high temperature hydrogen separation [8]. Most studies of TMCs are limited to high temperatures and few at room temperature. Even less available are the studies on mechanical behavior of VC and these are based on Knoop and Vickers microindentation [6, 9]. These studies are used to measure and determine the material hardness, hardness anisotropy, and infer the deformation mechanism. Given that these materials are promising for structural applications at low temperatures, it is surprising that there are no reports on mechanical responses of VC subjected to uniaxial loading at room-temperature. Here, as a first step, I focus on uniaxial microcompression of 001-oriented VC single-crystals at room-temperature to measure their strength, determine the extent of plasticity, and determine the deformation mechanism.

4.2 Results

4.2.1 VC(001)

Figure 4.1 shows representative SEM images from the bulk VC(001) single crystal of three sub-micron pillars, before (top panel) and after (bottom panel) compression. The SEM images are 10°-tilted views of the pillars with top diameters $D \approx$ a) 0.23 μm, b) 0.43 μm, and c) 0.75 μm. From these images, the height of the pillars noticeably decreased, while their average diameters increased upon compression, i.e. the pillars deformed plastically. Specifically, the pillar with the largest diameter, fig 4.1(c), is showing the largest changes in height and diameter and its shape can be described as a barrel. This behavior is typical of three out of five pillars with $D \approx 0.23$ μm, four out of five pillars ≈ 0.43 μm, and all five with $D \approx 0.75$ μm. The other two pillars deformed slightly followed by fracture. For the unfractured pillars their estimated plastic

strains are between 7 and 9% for $D \approx 0.23$ μm, 9 and 12% for $D \approx 0.43$ μm, and 2 and 20% for $D \approx 0.75$ μm.

Similarly, figure 4.2 shows representative SEM images from the bulk VC(001) single crystal of three intermediate sizes of pillars to those shown previously, before (top panel) and after (bottom panel) compression. The SEM images are 10°-tilted views of the pillars with top diameters D = a) 0.33 μm, b) 0.52 μm, and c) 0.59 μm. From these images, the height of the pillars noticeably decreased, while their average diameters increased upon compression, i.e. the pillars deformed plastically. This behavior is typical of two out of five pillars with $D \approx 0.33$ μm and three out of five pillars with ≈ 0.52 μm, and four out of five with $D \approx 0.61$ μm. The other pillars deformed slightly followed by fracture. For the unfractured pillars their estimated plastic strains are between 3 and 14% for $D \approx 0.33$ μm, 15 and 21% for $D \approx 0.52$ μm, and 9 and 21% for $D \approx 0.61$ μm.

Engineering stress vs. displacement data obtained during the *in situ* compression of all 30 pillars are plotted in Figures 4.1 and 4.2 in (d), (e), and (f) for their corresponding sizes. The $\sigma(\delta)$ data corresponding to the pillars in Figures 1 and 2 (a)-(c) are highlighted using red, green, and blue colors, respectively. In the initial region of the compression test I observe a linear elastic behavior, and the pillars undergo elastic deformation: δ increases linearly with increasing σ up to the yield point σ_y, followed by a smooth transition to non-linear plastic deformation for the smaller pillars with diameters up to $D \sim 0.43$ μm while an abrupt transition followed by the non-linear plastic deformation can be seen for the larger pillars having diameters $D \sim 0.52$ μm and greater. At $\sigma > \sigma_y$ I observe the following: 1) sudden drops in σ, large and small, due to displacement bursts, where the amplitudes appear to increase with decreasing D and 2) the rate

of strain hardening appears larger for pillars with diameters up to $D \sim 0.43$ μm than in those with diameters $D \sim 0.52$ μm and greater.

The yield strength σ_y of the 30 pillars is extracted from the σ vs δ curves in Figs 4.1 and 4.2 (d) – (f) and plotted as a function of D in Figure 4.3. From the profiles, the observed trend is that σ_y increases as the D decreases, from 12.7 ± 1.7 GPa for pillars with $D \approx 0.75$ μm to 18 ± 1 GPa for pillars with $D \approx 0.23$ μm. One data point in the largest diameter set is deviating from the trend and can be explained by looking at Fig 4.1(f). The compression test of the first pillar was a conservative effort and prematurely ended to preserve the pillar after observing a stress burst in the profile. The profile is the shortest in displacement, ~ 150 nm, of the five profiles. Consequently, the yield stress was underestimated from that profile and appears like an outlier.

To further characterize the observed behavior of size dependent plastic deformation, the compressed pillars were imaged with electron microscopy. Figures 4.4 and 4.5 are typical higher resolution SEM images obtained after compression of the same representative pillars from Figs 1 and 2 for each set with $D \approx$ 4(a) 0.23 μm, 4(b) 0.43 μm, 4(c) 0.43 μm, and 4(d) 0.75 μm and $D \approx$ 5(a) 0.33 μm, 5(b) 0.52 μm, and 5(c) 0.59 μm. In figs 4 and 5 all of the pillars exhibited localized plastic deformation shown by the slip bands from the top surface and leading across the body of the pillars with the exception of Figure 5(c). The pillar of Figure 5(c) with D = 0.59 μm did not show any slip bands, however, it plastically deformed likely due to deformation via continuous slip with minimal displacement amplitudes as seen in fig 4.2(f). Many of the pillars that were tested show clear evidence of slip and only a few do not. Dashed red, green, and blue lines, respectively, in Fig 4.4: (a), (b), (c) and (d) highlight the orientations of the slip bands with respect to the [001] pillar axes, where the angle shown is the angle between normal to the slip trace and the pillar axis and equivalently the angle between pillar axis normal surface and the slip

trace. In fig 4.4(a), the shear band is oriented at ~ 54°. Since the pillar axis is [001], the possible slip planes that are orientated at 54° with respect to the pillar axis belong to {111}. Based on this result, the operating slip system in this pillar is $\{111\}\langle 1\bar{1}0\rangle$. In fig 4(b), the slip band is oriented at ~ 45° with respect to the pillar axis [001] and suggests that the possible slip planes belong to {110}. Based on this result, the operating slip system in this pillar is $\{110\}\langle 1\bar{1}0\rangle$. Similarly, following the same argument for an orientation and its corresponding slip plane, the slip systems for the pillars shown in fig 4.4(c) and (d) and in fig 4.5(a) and (b) can also be identified as either a (110) slip plane if the orientation angle is ~ 45° or (111) slip plane if the orientation angle is ~ 54°. In all of the images of fig 4.4, two unique slip systems have been captured between the different sizes. Most interesting is the result that two different slip systems are also shown within two same sized pillars (D ~ 0.43 μm) and can be seen in figs 4.4(b) and (c). The range of pillar sizes helps facilitate the observation that a transition in slip system may occur based on the size of the crystal. Here I observed the slip plane change from (111) fig 4.4(a) in the smallest pillar (0.23 μm) to (110) for a larger pillar fig 4.5(a) (0.33 μm) to both (110) and (111) for larger pillars of fig 4.4(b) and (c) (0.43 μm), respectively, to (110) for larger pillars fig 4.5(b) 0.52 μm, and fig 4.4(d) of 0.75 μm. This change in slip system is opposite to that observed in NbC. Here the VC slip system changes from the (111) glide plane to (110) as crystal size increases, while the NbC slip system changes from the (110) glide plane to (111) with increasing crystal size.

Fig 4.4(e) is a typical bright TEM image acquired from the FIB-milled electron-transparent cross-section of the compressed pillar with D ~ 0.43 μm, shown in fig 4.4(c). The inset in fig 4.4(e) is a selected area electron diffraction (SAED) pattern obtained from the same field of view with zone axis z = $\{\bar{1}12\}$. Note that both the TEM image and the SAED in fig 4.4(e) are obtained using the same sample/beam tilt. VC {220} and {111} reflections are

highlighted using yellow and green circles, respectively. The observed 2-fold symmetry of the diffraction spots and the absence of any other reflections indicate that the compressed pillar remains single-crystalline with B1 structure. That is, I do not observe any deformation induced lattice distortions, phase transformation, and/or twinning in the pillar. Therefore, I do not expect any deviations in the orientation of the crystal planes measured from the images. Slip traces are also found in the images, which appear as darker contrast parallel sets of lines. Green arrows in fig 4.4(e) are drawn perpendicular to the visible slip traces. A dashed green line in fig 4.4(e) inset is drawn passing through the (000) central and {111} diffraction spots in the SAED. The dashed green line is then transferred to the TEM and placed over the largest slip trace along with a solid green line that is perpendicular. The solid green line is parallel to the observed slip trace and corresponds to the {111} slip planes. This is consistent with our angle based identification of the {111} slip trace from the SEM image in fig 4.4(c). Based on these measurements, I conclude that the slip traces observed in the TEM image are due to {111} planes. With the assumption that $\langle 1\bar{1}0 \rangle$ is the slip direction, generally expected in B1 crystals, these results indicate the operation of both $\{110\}\langle 1\bar{1}0 \rangle$ and $\{111\}\langle 1\bar{1}0 \rangle$ slip systems.

4.2.2 VC(110)

Figure 4.6 shows representative SEM images from the bulk VC(110) single crystal of three sub-micron pillars, before (top panel) and after (bottom panel) compression. The SEM images are 10°-tilted views of the pillars with top diameters D = a) 0.28 μm, b) 0.46 μm, and c) 0.75 μm. From these images, the height of the pillars and their average diameters slightly changed upon compression. Furthermore, a more typical observation of all the pillars is the formation of slip bands at the top section i.e., the pillars experienced local plastic deformation.

Specifically, the pillar with the largest diameter, fig 4.6(c), is showing the greatest amount of plastic deformation and the largest slip bands. This behavior is typical of all five pillars with $D \approx 0.27$ μm and three out of five with $D \approx 0.47$ μm, and three out of five with $D \approx 0.75$ μm. The other two pillars in each size deformed slightly followed by fracture. For the unfractured pillars their estimated plastic strains are between 5 and 7% for $D \approx 0.27$ μm, 1 and 9% for $D \approx 0.47$ μm, and 2 and 14% for $D \approx 0.75$ μm.

Engineering stress vs. displacement data obtained during the *in situ* compression of all 14 pillars are plotted in Figure 4.6(d), (e), and (f) for their corresponding sizes. The $\sigma(\delta)$ data corresponding to the pillars in Figures 4.6(a)-(c) are highlighted using red, green, and blue colors, respectively. During the initial stages of loading, the profile indicates a linear elastic behavior: δ increases linearly with increasing σ up to the yield point σ_y, and a non-linear plastic deformation region is not observed. At $\sigma > \sigma_y$ I observe the following: 1) sudden drops in σ with a large displacement increase indicating a large slip event or sudden fracture i.e., the pillars exhibit brittle behavior.

The yield strength σ_y of the 14 pillars is extracted from the σ vs δ curves in Fig 4.6(d) – (f) and plotted as a function of D in Figure 4.7. From the profiles, the observed trend is that σ_y increases as the D decreases, from 17.4 ± 1.3 GPa for pillars with $D \approx 0.75$ μm to 22.9 ± 0.9 GPa for pillars with $D \approx 0.27$ μm. One data point in the smallest diameter set is missing from the trend. The first pillar was damaged prior to the compression test and eliminated from the data set.

To further characterize the observed behavior of size dependent plastic deformation, the compressed pillars were imaged with electron microscopy. Figure 4.8 (a-c) are typical higher resolution SEM images obtained after compression of the same representative pillars from Figure

4.6 with $D \approx$ 4.6(a) 0.28 μm, 4.6(b) 0.46 μm, and 4.6(c) 0.75 μm. In fig 4.8 all of the pillars exhibited localized plastic deformation shown by the slip bands at the top surface and in fig 4.8(c) the pillar also has slip bands across the body of the pillar. Many of the pillars that were tested show clear evidence of slip and only one or two in each set fractured. Dashed red, green, and blue lines, respectively, in Fig 4.8: (a), (b), and (c) highlight the orientations of the slip bands with respect to the [110] pillar axes, where the angle shown is the angle between normal to the slip trace and the pillar axis and equivalently the angle between pillar axis normal surface and the slip trace. In fig 4.8(a-c), the shear bands are oriented at ~ 35°. Since each pillar axis is [110], the possible slip planes that are orientated at 35° with respect to the pillar axis belong to {111}. Based on this result, the operating slip system in these pillars is $\{111\}\langle 1\bar{1}0\rangle$. In all of the images of fig 4.8, only one unique slip system has been captured between the different sizes. The range of pillar sizes help to identify that a transition in slip system does not occur based on the size of the crystals.

4.2.3 VC(111)

Figure 4.9 shows representative SEM images from the bulk VC(111) single crystal of three sub-micron pillars, before (top panel) and after (bottom panel) compression. The SEM images are 10°-tilted views of the pillars with top diameters $D \approx$ a) 0.25 μm, b) 0.44 μm, and c) 0.74 μm. From these images, the height of the pillars noticeably decreased, while their average diameters increased upon compression, i.e. the pillars deformed plastically. Furthermore, a more common observation of all the pillars is the formation of slip bands at the top section and across the body of the pillars i.e., the pillars experienced plastic deformation, and can be seen in fig 4.9(a) and (c). Also, the pillar with the largest diameters, fig 4.9(c), is showing the greatest

amount of plastic deformation and more slip bands than the smaller pillars. This behavior is typical of all five pillars with $D \approx 0.24$ μm and all five with $D \approx 0.44$ μm, and four out of five with $D \approx 0.74$ μm. The other pillar in the largest size deformed and fractured. For the unfractured pillars their estimated plastic strains are between 10 and 20% for $D \approx 0.24$ μm, 4 and 12% for $D \approx 0.44$ μm, and 9 and 12% for $D \approx 0.74$ μm. Here the smallest pillars seem to experience the greatest amount of plastic deformation, however, the other pillars could have been further compressed and also experienced extended plastic deformation. The goal was also to preserve the pillars to characterize their slip systems, and this prevented the extended compression times.

Engineering stress vs. displacement data obtained during the *in situ* compression of all 15 pillars are plotted in Fig 4.9(d), (e), and (f) for their corresponding sizes. The $\sigma(\delta)$ data corresponding to the pillars in Fig 4.9(a), (b), and (c) are highlighted using red, green, and blue colors, respectively. During the initial stages of loading, the profiles indicate a linear elastic behavior: δ increases linearly with increasing σ up to the yield point σ_y, followed by a smooth transition to non-linear plastic deformation for all pillars. At $\sigma > \sigma_y$ I observe the following: 1) small and large frequent drops in σ due to displacement bursts, where the amplitudes appear to increase with decreasing D and 2) the rate of strain hardening appears to increase with decreasing D.

The yield strength σ_y of the 15 pillars is extracted from the σ vs δ curves in Fig 4.9 (d) – (f) and plotted as a function of D in Figure 4.10. From the profiles, the observed trend is that σ_y increases as the D decreases, from 16.1 ± 0.8 GPa for pillars with $D \approx 0.74$ μm to 23.0 ± 0.6 GPa for pillars with $D \approx 0.24$ μm. All pillars are included in the data set for the (111) surface orientation.

To further characterize the observed behavior of size dependent plastic deformation, the compressed pillars were imaged with electron microscopy. Figure 4.11 (a), (c), and (d) are typical higher resolution SEM images obtained after compression of the same representative pillars from Figure 4.9 with $D \approx$ 9(a) 0.25 μm, 9(b) 0.44 μm, and 9(c) 0.74 μm. Fig 4.11(b) is a second pillar of the smallest size having also a $D \approx$ 0.25 μm. In fig 4.11 all of the pillars exhibited plastic deformation shown by the slip bands across the body of the pillars and in fig 4.11(d) the pillar also has multiple slip bands across the body of the pillar and is a great example for the comparisons of size differences. All of the pillars that were tested show clear evidence of slip and only one pillar in the largest diameter size set fractured. Dashed red, green, and blue lines, respectively, in fig 4.11(a) and (b), (c), and (d) highlight the orientations of the slip bands with respect to the [111] pillar axes, where the angle shown is the angle between normal to the slip trace and the pillar axis and equivalently the angle between pillar axis normal surface and the slip trace. Following the same procedure of measuring the angle of the slip band as in figs 4.4, 4.5, and 4.8 I can identify the slip system for each pillar. In fig 4.11(a) the two large parallel shear bands are oriented at ~ 54°, indicating a (001) slip plane, and a smaller shear band can be seen near the top surface. In fig 4.11(b) a large slip band can be seen across the entire body of the pillar at ~ 35°, indicating a (110) slip plane, as well as multiple parallel slip bands near the top of the pillar but are not seen across the body of the pillar. Also, in fig 4.11(b) a slip band is seen at the top of the pillar on the backside and is responsible for detaching a majority of the top of the pillar. In fig 4.11(c) I observe two different orientations of the slip bands. A large slip band across the entire body of the pillar at ~ 54° and several faint slip traces are present on the surface at ~ 70°, indicating that the (001) and (111) respective slip planes, are active. In fig 4.11(d)

multiple parallel slip bands are present across the entire body of the pillar at ~ 54°, indicating a (001) slip plane, and a shear band is present at the top left side.

Overall, since each pillar axis is [111], the three different angles indicate the three slip planes are active. Based on this result, the operating slip systems in these pillars are $\{001\}\langle 1\bar{1}0\rangle$, $\{110\}\langle 1\bar{1}0\rangle$, $\{111\}\langle 1\bar{1}0\rangle$. Furthermore, the range of pillar sizes help to observe that a common slip system, $\{001\}\langle 1\bar{1}0\rangle$, occurs throughout the three sizes of crystals.

The yield strengths σ_y of the 59 pillars from all orientations in Figures 4.3, 4.7, and 4.10 are combined and plotted as a function of *D* in Figure 4.12. From the profiles, the observed trend is that σ_y increases as the *D* decreases and each orientation does so at different rates.

4.3 Discussion

The operation of the $\{110\}\langle 1\bar{1}0\rangle$ and $\{111\}\langle 1\bar{1}0\rangle$ slip systems have been reported on during microindentation of bulk VC(001) and other group 5 TMC(001) single-crystals at ambient and elevated temperatures [6], respectively. However, I note that there are no reports of the activation of two slip systems during room-temperature compression of 001-oriented group 5 TMC crystals except in our previous report on NbC(001) [10]. Additionally, there are no reports of the activation of multiple slip systems during room-temperature compression of 110- and 111-oriented group 5 TMC crystals. Furthermore, previous reports identified $\{110\}\langle 1\bar{1}0\rangle$ as the only slip system during uniaxial compression of 001-oriented single-crystalline TaC pillars with D < 0.5 μm [11] while in 110-oriented Ta-C-N pillars, $\{111\}\langle 1\bar{1}0\rangle$ is found to be the only active slip system [12]. The differences between the two group 5 TMCs can possibly be explained when considering their pillar sizes, crystal orientation, C-content, and loading rates. Here I have again

observed the activation of multiple slip systems in three different crystal orientations of sub-micron pillars, also the simultaneous activation of two slip systems within the same pillar, and three slip systems within one crystal orientation.

During compression of the pillars, yielding occurred via slip either by one or a combination of the following descriptions: locally at the top surface, across the body of the pillar, through multiple parallel slip bands creating multiple slip steps on the surface of the pillar, and/or continuously throughout the pillar as diffuse slip, allowing for extensive plastic deformation seen as the barreling effect on the larger pillars. From the post compression morphology shown in Figures 4.4(a-c), 4.5(a), 4.8(a) and (b), and 4.11(a) and (b), it is apparent that I can observe localized deformation as shear bands on the top surfaces. In the pillars of Figures 4.4(d), 4.5(b), 4.8(c), and 4.11(a-d) I observe the shear bands across the body of the pillars. In the pillars of Figures 4.1(c), 4.2(b) and (c), and 4.9(c) I observe barreling of the pillars. The observed behaviors are characteristic of plastic deformation that is typically observed in FCC bulk and microcrystals of metals [13]. The localized deformation behavior is typically observed in ionic crystals [14].

The explanation that was presented for the NbC(001) results [10] also applies for the VC pillars. That is, the number of dislocations and/or dislocation sources scales with pillar size. In smaller size pillars ($D \approx 0.25$ μm), the number of dislocations (and/or sources) within the pillar is expected to be low and plastic deformation is likely to be controlled by the surface nucleation of dislocations [15] along energetically the most favorable slip system. As a result, slip events are expected to be finite and discontinuous resulting in displacement bursts with larger amplitudes and higher yield strength. With increasing pillar size, both surface nucleation and multiplication of internal dislocations lead to higher number of dislocations and the activation of a second slip

system $\{110\}\langle 1\bar{1}0\rangle$, which results in more continuous slip with smaller amplitude displacement bursts, larger plastic strain, and lower yield strength. For the VC(001) crystal, inherent in my model is the speculation that the $\{111\}\langle 1\bar{1}0\rangle$ and $\{110\}\langle 1\bar{1}0\rangle$ slip systems are dominant in relatively smaller and large-size crystals, respectively. In the case for VC(110) crystal the $\{111\}\langle 1\bar{1}0\rangle$ slip system is the only one activated for all sizes and is therefore the dominant slip system. In VC(111) a combination of the three slip systems can be active depending on size. For example, the $\{001\}\langle 1\bar{1}0\rangle$ and $\{110\}\langle 1\bar{1}0\rangle$ slip systems are active for the set of pillars with $D \approx$ 0.24 μm, the $\{001\}\langle 1\bar{1}0\rangle$ and $\{111\}\langle 1\bar{1}0\rangle$ slip systems are active for the set of pillars with $D \approx$ 0.44 μm, and only the $\{001\}\langle 1\bar{1}0\rangle$ slip system is active for the set of pillars with $D \approx 0.74$ μm. I note that the $\{001\}\langle 1\bar{1}0\rangle$ slip system is active for all sizes indicating a dominant role.

The aforementioned observations indicate that the three crystal orientations of VC, 001, 110, and 111 are experiencing plasticity or brittle behavior. To elaborate, the VC(001) pillars experience the most plastic deformation as characterized by their σ-ε curves in Figs 4.1 and 4.2(d-f) and are considered plastic with the ability to sustain extended plastic deformation with larger diameters $D \approx 0.75$ μm. The VC(110) pillars do not experience plastic deformation as characterized by their σ-ε curves in Figs 4.6(d-f) and are considered brittle in these experiments. The VC(111) pillars also experience plastic deformation as characterized by their σ-ε curves in Figs 4.1 and 4.9(d-f) and are considered plastic with the ability to sustain further plastic deformation (but limited compared to VC(001) pillars) with larger diameters $D \approx 0.74$ μm.

The possibility that a transition in slip system may occur based on the size of the crystal was further explored here in the VC(001) crystal by including more pillar sizes within the sub-micron range. This is supported for the 001 orientation with a larger range of sizes because I

again observe only one slip system, $\{111\}\langle 1\bar{1}0\rangle$, for the smallest pillars ($D \approx 0.25$ μm) and a transition occurs at ($D \approx 0.43$ μm) where two slip systems are activated $\{111\}\langle 1\bar{1}0\rangle$ and $\{110\}\langle 1\bar{1}0\rangle$, followed by the activation of only the second slip system $\{110\}\langle 1\bar{1}0\rangle$ in the larger pillars for $D \geq 0.52$ μm. In the VC(110) crystal a transition is not observed because only one slip system is active within the sub-micron range. The VC(111) pillars have the most interesting behavior since three slip systems are identified as active. A transition in slip system is not necessarily observed, rather a combination of slip systems occurs throughout the sub-micron range. The (001) and (110) slip planes are present for pillars with $D \approx 0.24$ μm while the (001) and the (111) slip planes are present for pillars with $D \approx 0.44$ μm. The (001) slip plane is present in all three sizes and contributes to the plastic nature of the VC(111) pillars as seen in Figure 4.11.

Figure 4.12 compares the mechanical yield strengths of the three pillar orientations. Clearly, there is an increase in yield strength as the diameter is decreased for all orientations and at different rates for each orientation. The strength of the VC(001) pillars increases the least and is considered the “soft” orientation, relatively speaking, because earlier it was described that the VC(001) pillars experienced the most plastic deformations and extended deformation in the larger pillars. The strength of the VC(110) pillars increases at the highest rate and is considered the “hard” orientation because earlier it was stated that the VC(110) pillars did not experience plastic deformation and was described as brittle. The strength of the VC(111) pillars also increases at a higher rate than VC(001) pillars and is characterized as having dual behavior of both VC(001) and VC(110) pillars. Specifically, the VC(111) pillars have the combination of allowing for plastic deformation similar to VC(001) pillars and higher yield strengths like that of

VC(110) pillars compared to VC(001) pillars making it the orientation of choice for mechanical applications.

4.4 Conclusion

The micromechanical responses of VC with 001, 110, and 111 orientations were carried out to characterize each and determine their active slip systems. In situ SEM based compression of cylindrical VC(001) pillars with sub-micrometer size diameters revealed that the pillars deform plastically with large strains and diameter-dependent yield strengths that increase with decreasing diameter. From the SEM images, I have identified the operation of up to three slip systems dependent on the crystal orientation along with the observation of a transition in slip system for the 001 orientation. The 110 orientation is the hardest of the three because it does not exhibit plastic deformation and is described as brittle. The 111-oriented pillars also experience plastic deformation and are considered plastic with the ability to sustain further plastic deformation (but limited compared to VC(001) pillars) with larger diameters.

Based on these results, I suggest that the large plasticity in VC crystals at room-temperature is a direct consequence of the simultaneous presence of multiple slip systems within the respective orientation. These results again support the exciting possibility of designing refractory TMCs with superior plasticity by optimizing the grain size, orientations, and compositions that promotes the activation of single or multiple desired slip systems.

4.5 Figures

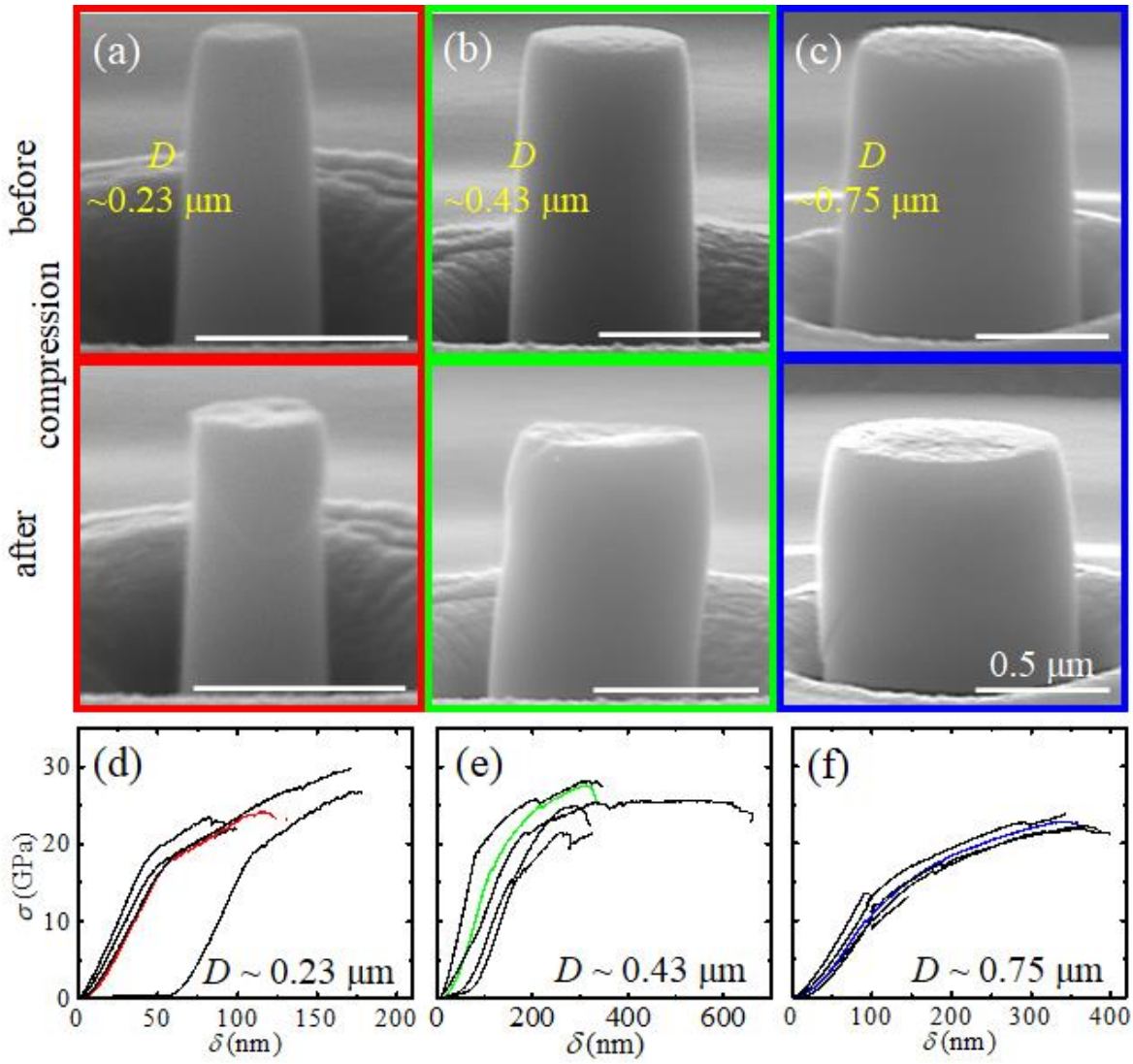

Figure 4.1: (a-c) Representative SEM images acquired from the bulk VC(001) with pillars of top diameters D = a) 0.23 μm, b) 0.43 μm, and c) 0.75 μm before (top panel) and after compression (bottom panel). (d-f) Plots of engineering stress (σ) vs. displacement (δ) data obtained during *in situ* compression of three sets of pillars with D around (d) 0.23 μm, (e) 0.43 μm, and (f) 0.75 μm. The $\sigma(\delta)$ data corresponding to the pillars in (a), (b), and (c) are shown using red, green, and blue curves, respectively.

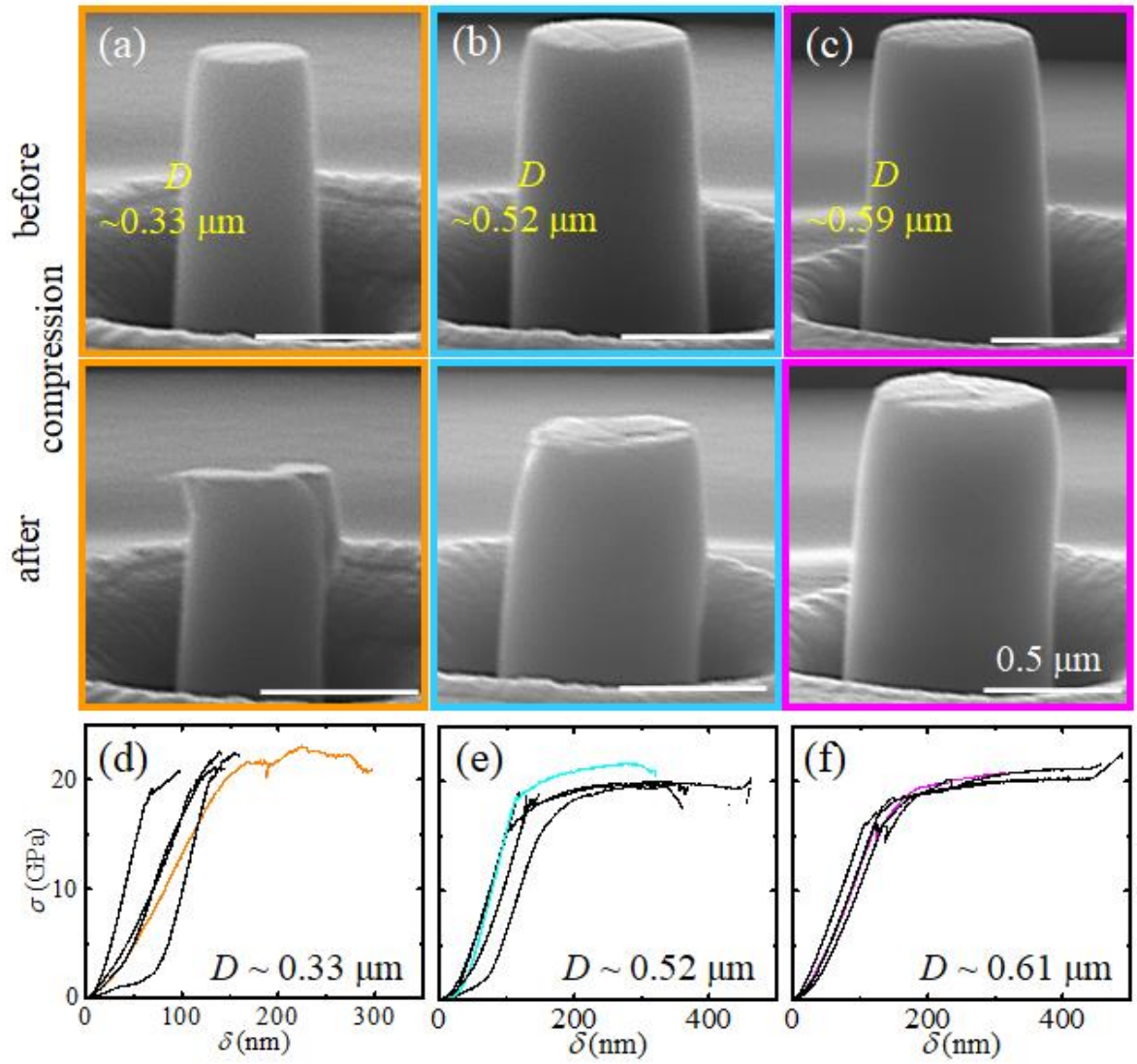

Figure 4.2: (a-c) Representative SEM images acquired from the bulk VC(001) with pillars of top diameters D = a) 0.33 μm, b) 0.52 μm, and c) 0.59 μm before (top panel) and after compression (bottom panel). (d-f) Plots of engineering stress (σ) vs. displacement (δ) data obtained during *in situ* compression of three sets of pillars with D around (d) 0.33 μm, (e) 0.52 μm, and (f) 0.61 μm. The $\sigma(\delta)$ data corresponding to the pillars in (a), (b), and (c) are shown using orange, cyan, and magenta curves, respectively.

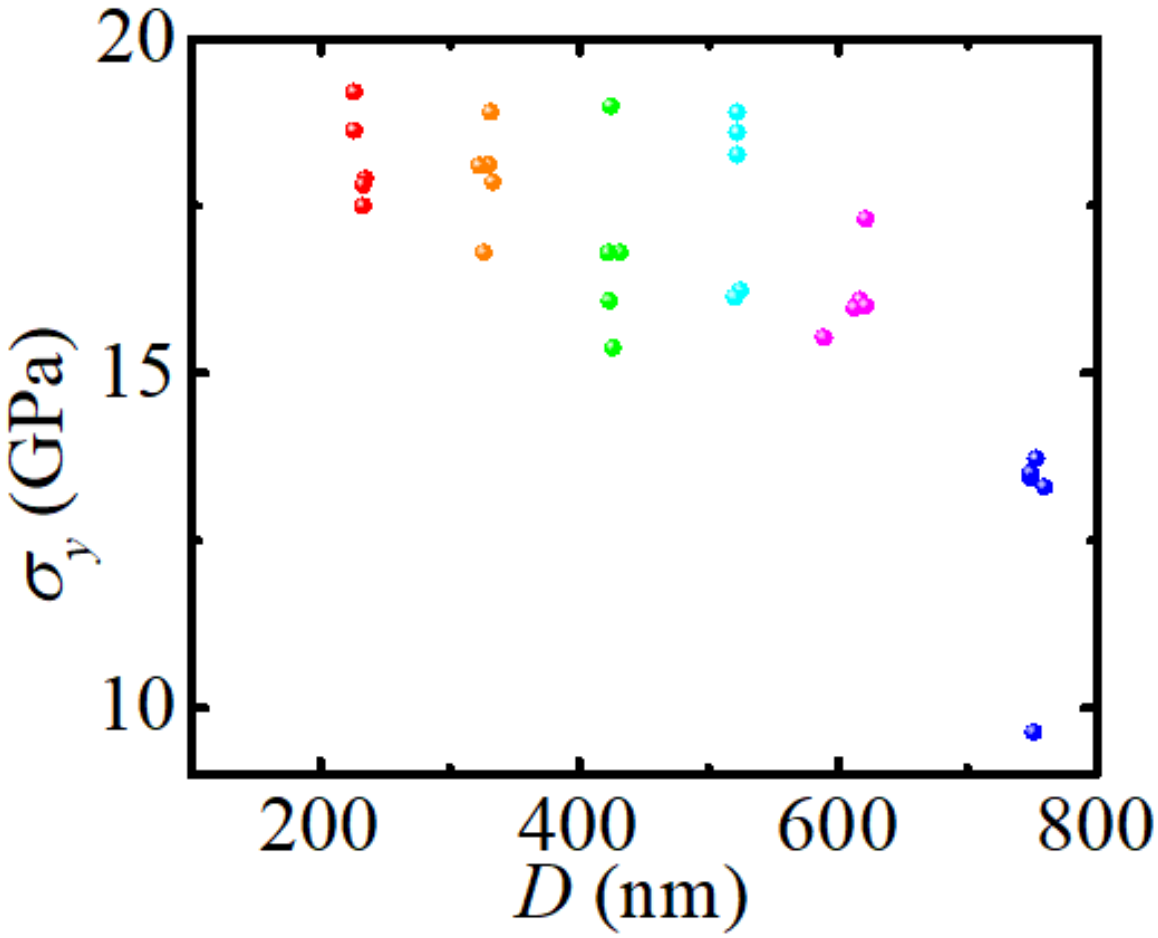

Figure 4.3: Plot of yield strengths σ_y vs. D, extracted from compression tests of all VC(001) pillars from Figures 4.1 and 4.2, ranging in diameter from 0.23 to 0.76 μm.

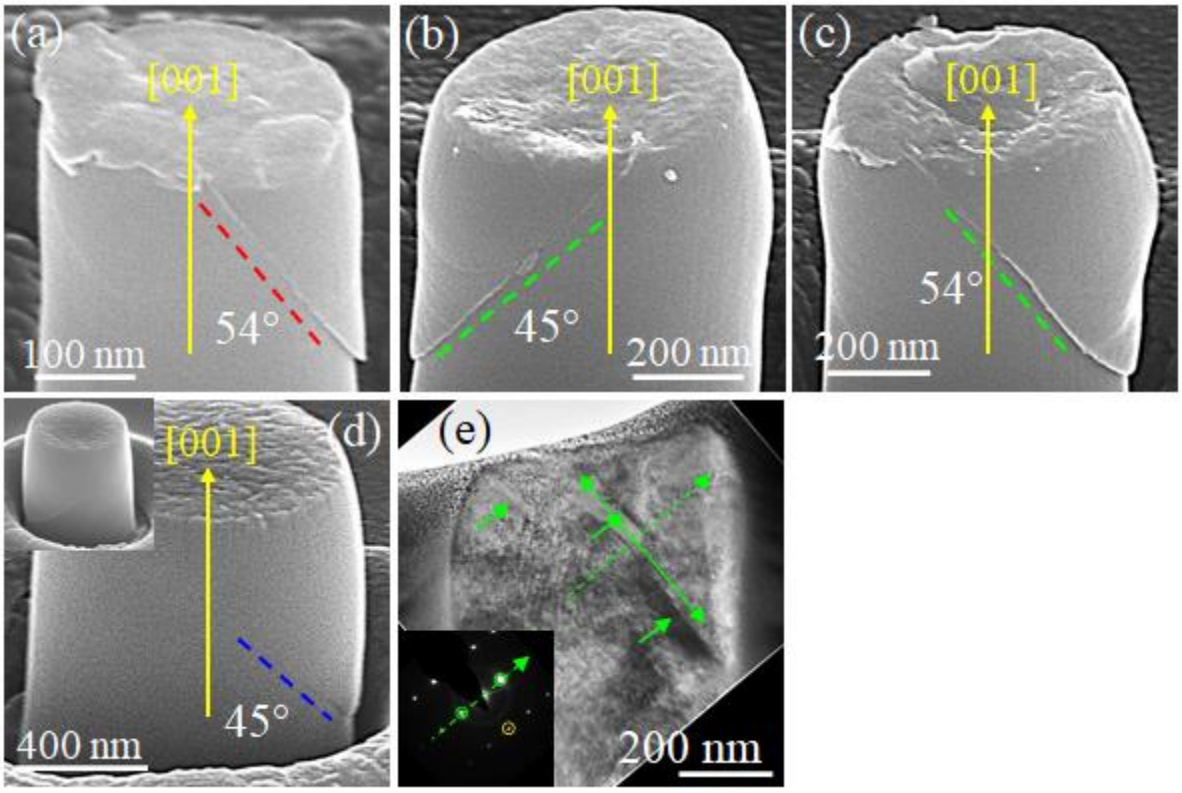

Figure 4.4: (a-d) Typical SEM images (60°-tilt) acquired after the compression of four different VC(001) pillars with $D \approx$ (a) 0.23 μm, (b) 0.43 μm, (c) 0.43 μm, and (d) 0.75 μm. Dashed red, green, and blue lines, respectively, in (a), (b), (c) and (d) highlight the orientations of the slip bands with respect to the [001] pillar axes, where the angle shown is the angle between normal to the slip trace and the pillar axis and equivalently the angle between pillar axis normal surface and the slip trace. In (d), the inset image is a rotated view of the pillar's opposite side. (e) Representative bright field transmission electron microscopy (TEM) image obtained from an electron-transparent cross-section of the compressed pillar shown here in (c). Associated selected area electron diffraction (SAED) pattern with zone axis z = $\{\bar{1}12\}$ of the same area of the pillar is shown as inset. Green and yellow circles indicate VC {111} and {220} reflections, respectively. Dashed green line is drawn passing through the central (000) spot and {111} diffraction spots in the SAED. Dashed green line is transferred to the image and a perpendicular solid green line is drawn indicating the parallel slip plane is the (111). Several other darker contrast parallel sets of lines are highlighted by green arrows and are identified as (111) slip planes.

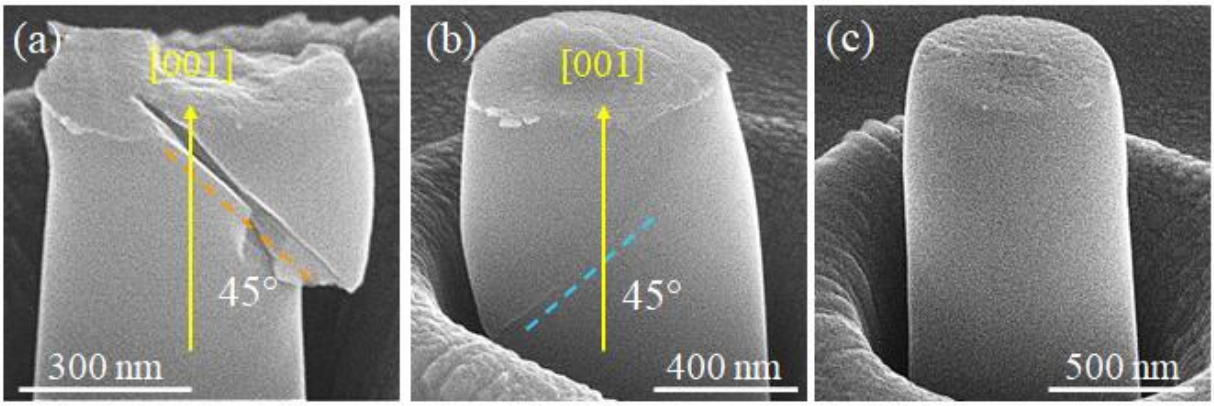

Figure 4.5: (a-c) Typical SEM images (60°-tilt) acquired after the compression of three different VC(001) pillars with $D \approx$ (a) 0.33 μm, (b) 0.52 μm, and (c) 0.59 μm. Dashed orange and cyan lines, respectively, in (a) and (b) highlight the orientations of the slip bands with respect to the [001] pillar axes, where the angle shown is the angle between normal to the slip trace and the pillar axis and equivalently the angle between pillar axis normal surface and the slip trace.

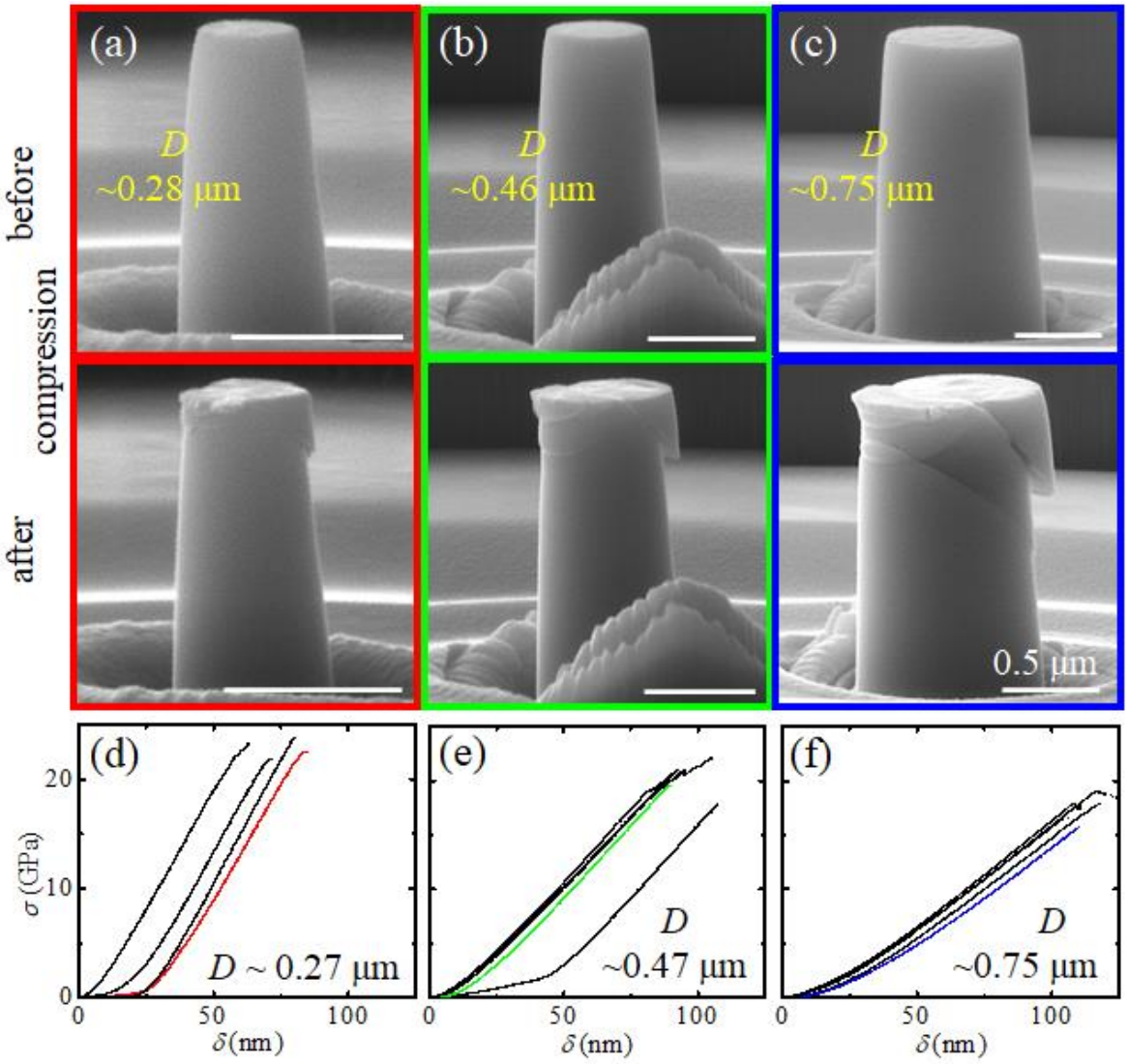

Figure 4.6: (a-c) Representative SEM images acquired from the bulk VC(110) with pillars of top diameters D = a) 0.28 μm, b) 0.46 μm, and c) 0.75 μm before (top panel) and after compression (bottom panel). (d-f) Plots of engineering stress (σ) vs. displacement (δ) data obtained during *in situ* compression of three sets of pillars with D around (d) 0.27 μm, (e) 0.47 μm, and (f) 0.75 μm. The $\sigma(\delta)$ data corresponding to the pillars in (a), (b), and (c) are shown using red, green, and blue curves, respectively.

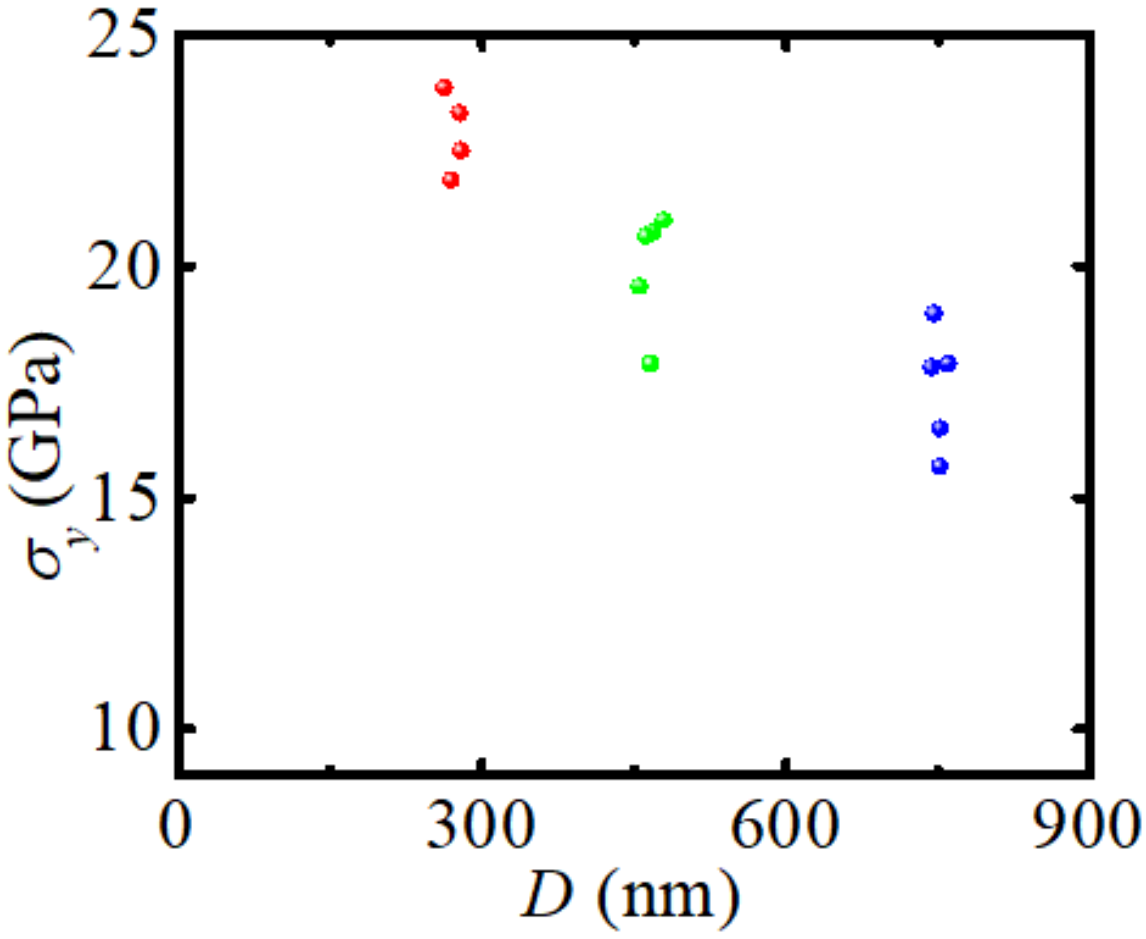

Figure 4.7: Plot of yield strengths σ_y vs. D, extracted from compression tests of all VC(110) pillars from Figure 4.6, ranging in diameter from 0.25 to 0.76 μm.

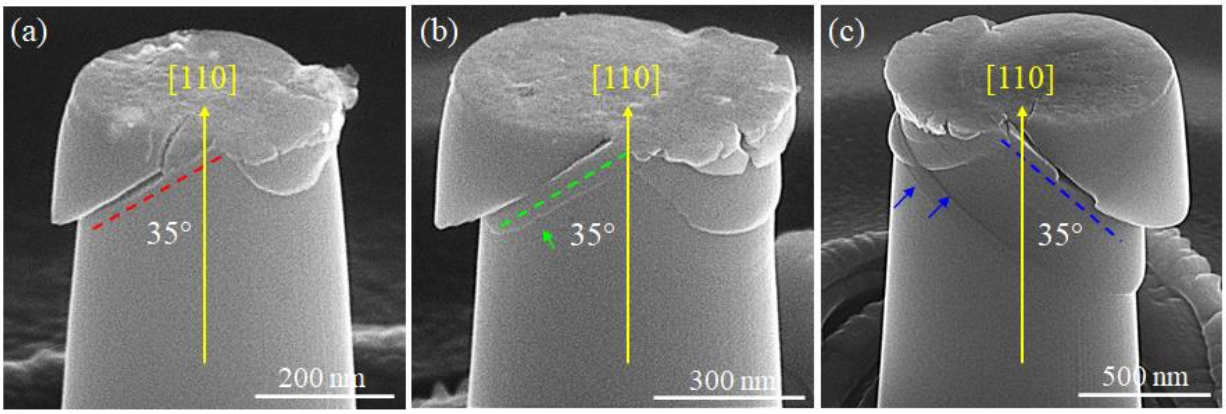

Figure 4.8: (a-c) Typical SEM images (60°-tilt) acquired after the compression of three different VC(110) pillars with $D \approx$ (a) 0.28 μm, (b) 0.46 μm, and (c) 0.75 μm. Dashed red, green, and blue lines, respectively, in (a), (b), and (c) highlight the orientations of the slip bands with respect to the [001] pillar axes, where the angle shown is the angle between normal to the slip trace and the pillar axis and equivalently the angle between pillar axis normal surface and the slip trace.

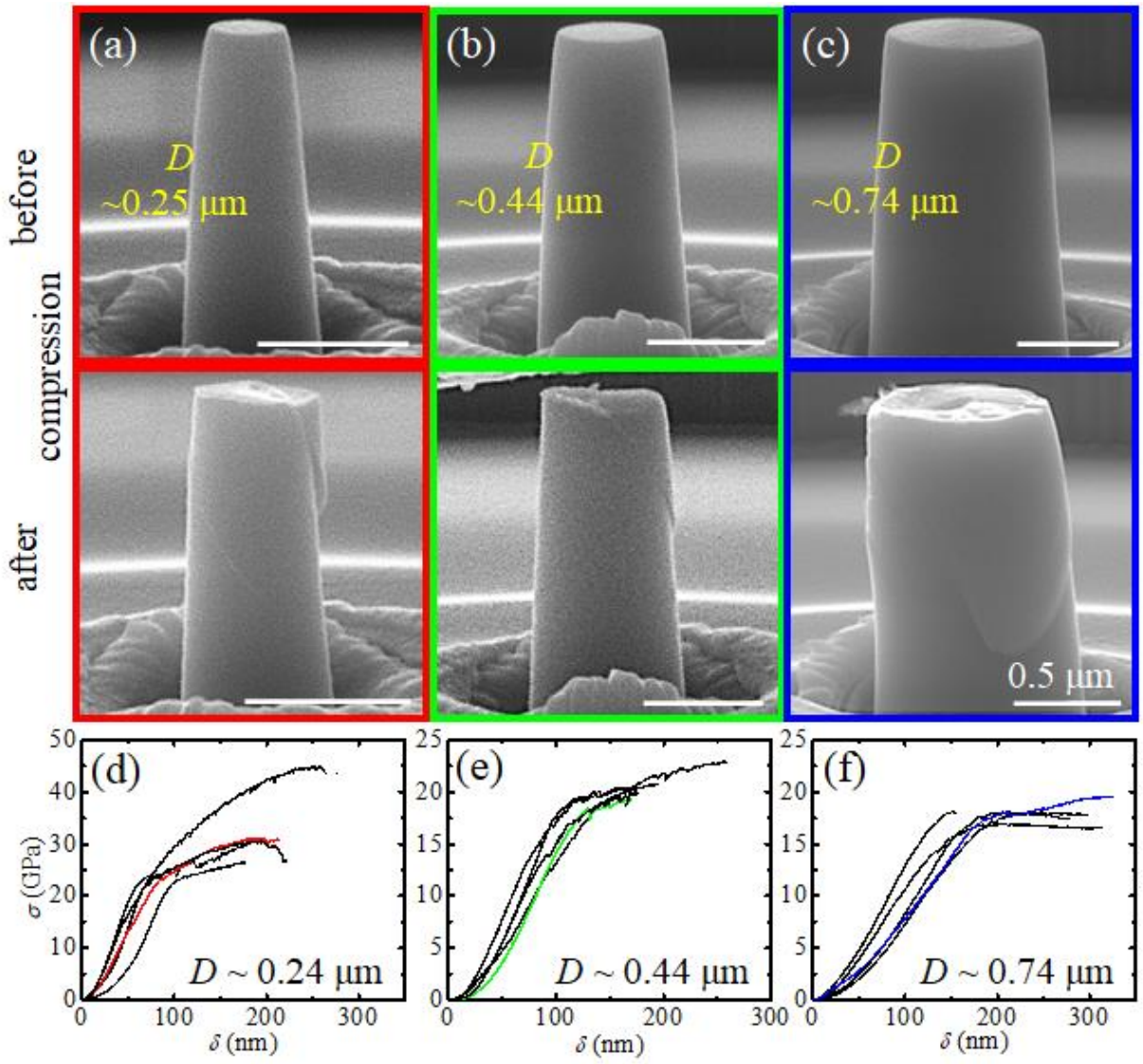

Figure 4.9: (a-c) Representative SEM images acquired from the bulk VC(111) with pillars of top diameters D = a) 0.25 μm, b) 0.44 μm, and c) 0.74 μm before (top panel) and after compression (bottom panel). (d-f) Plots of engineering stress (σ) vs. displacement (δ) data obtained during *in situ* compression of three sets of pillars with D around (d) 0.24 μm, (e) 0.44 μm, and (f) 0.74 μm. The $\sigma(\delta)$ data corresponding to the pillars in (a), (b), and (c) are shown using red, green, and blue curves, respectively.

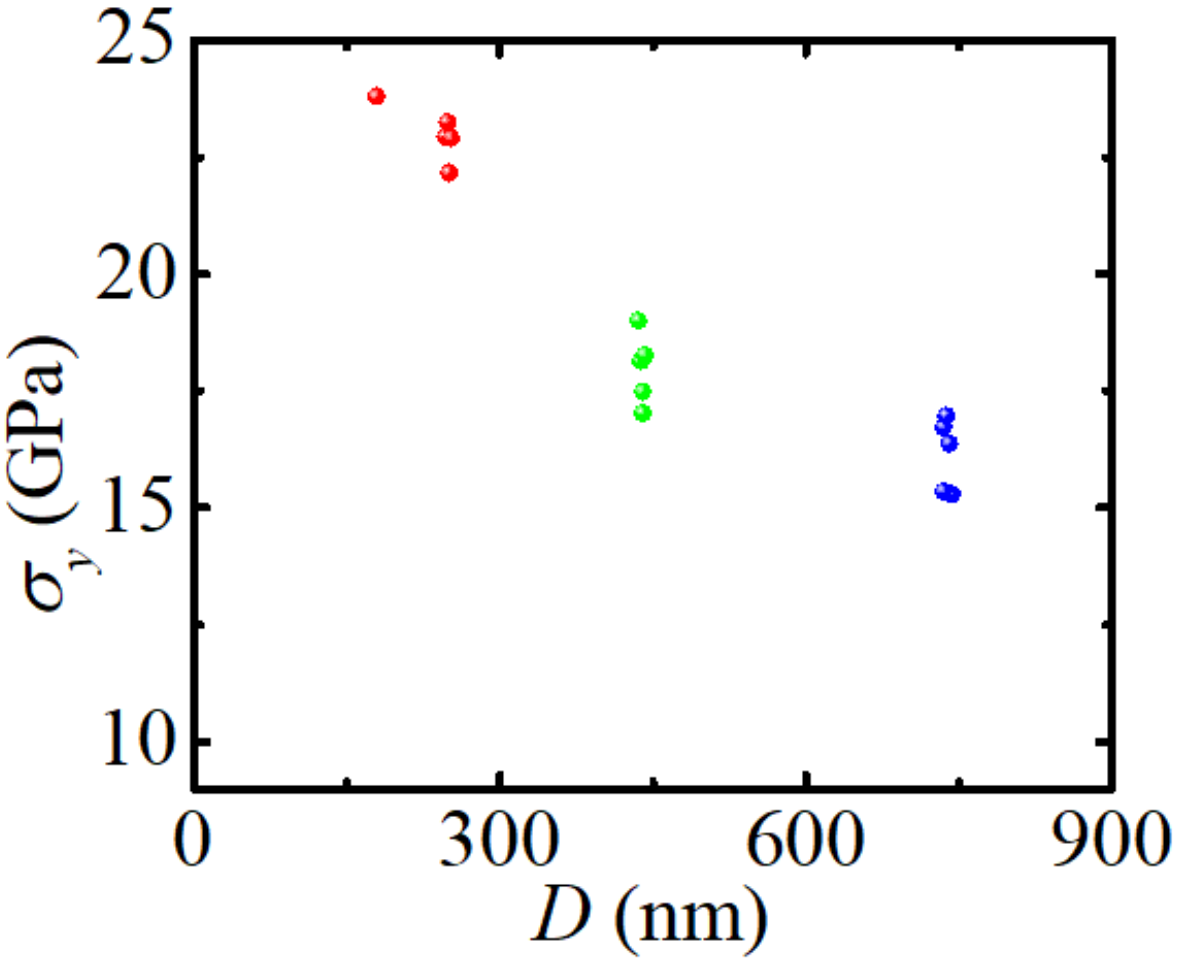

Figure 4.10: Plot of yield strengths σ_y vs. D, extracted from compression tests of all VC(111) pillars from Figure 4.9, ranging in diameter from 0.18 to 0.74 μm.

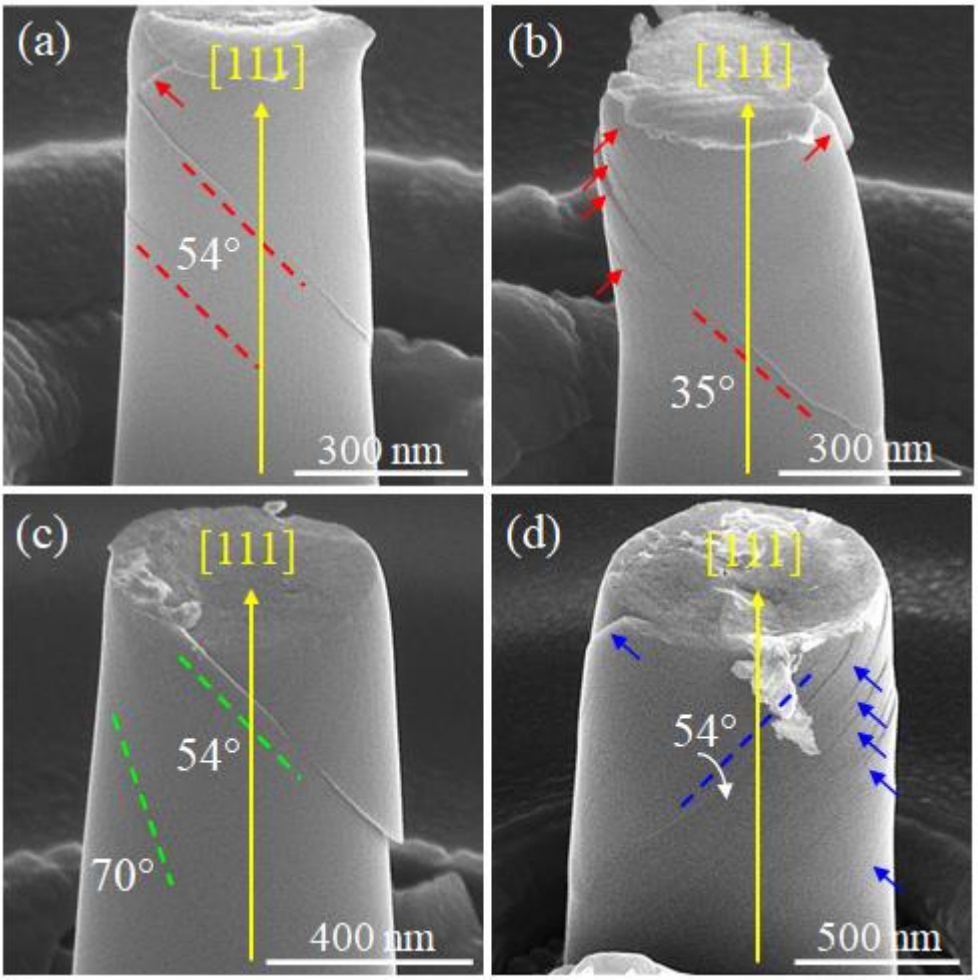

Figure 4.11: (a-c) Typical SEM images (60°-tilt) acquired after the compression of four different VC(111) pillars with $D \approx$ (a) 0.25 μm, (b) 0.25 μm (c) 0.44 μm, and (d) 0.74 μm. Dashed red, green, and blue lines, respectively, in (a), (b), (c), and (d) highlight the orientations of the slip bands with respect to the [001] pillar axes, where the angle shown is the angle between normal to the slip trace and the pillar axis and equivalently the angle between pillar axis normal surface and the slip trace. Note that here in Figure 4.11(c) there are several faint slip traces present on the surface of the pillar above and parallel to the 70° dashed green line.

Table 4.1: Slip planes and corresponding Schmidt factors based on a $\langle 1\bar{1}0 \rangle$ slip direction. ϕ is the angle between the slip plane normal and the loading direction. *This slip plane can only be activated in the $\langle 001 \rangle$ slip direction.

Loading Direction	Slip Plane	Schmidt Factor	ϕ (deg.)
[001]	{001}	0	0
	{110}	0.5	45
	{111}	0.408	54.7
[110]	{001}	0.353	45
	{110}	0.25	60
	{111}	0.408	35.3
[111]	{001}	0.471	54.7
	{110}	0, 0.408*	0, 35.3*
	{111}	0.272	70.5

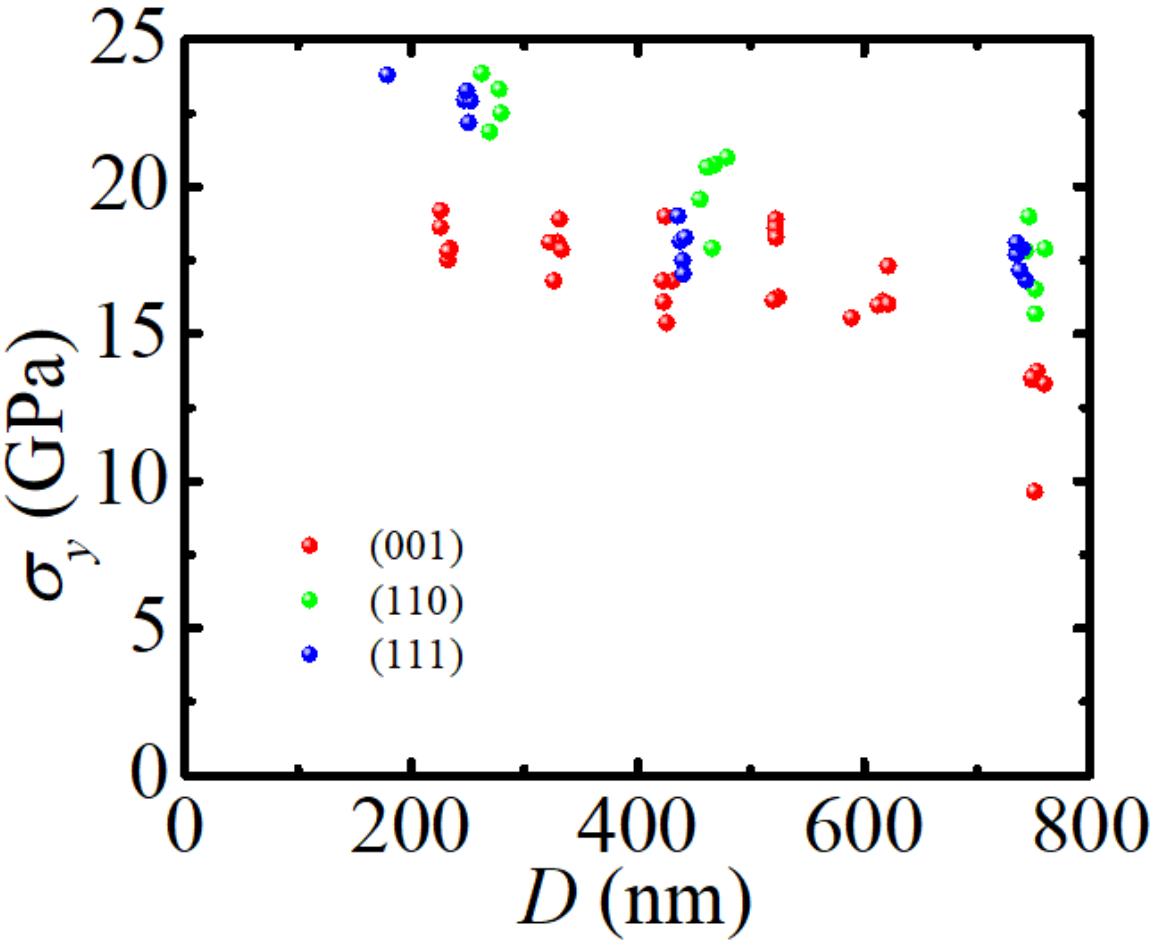

Figure 4.12: Plot of yield strength σ_y vs. D, summarizing all compression tests of VC (001), (110), and (111) pillars ranging in diameter from 0.18 to 0.74 μm from Figures 4.3, 4.7, and 4.10.

References

1. L.E. Toth, *Transition metal carbides and nitrides*. 1971, New York: Academic Press.

2. W.S. Williams, *Transition-metal carbides.* Progress in Solid State Chemistry, 1971. **6**: p. 57-118.

3. H.O. Pierson, *Handbook of Refractory Carbides and Nitrides: Properties, Characteristics, Processing, and Applications*. 1996: William Andrew Publishing/Noyes.

4. R.H.J. Hannink, D.L. Kohlstedt, and M.J. Murray, *Brittle-Region Slip Systems in the Transition-Metal Carbides.* physica status solidi (a), 1971. **6**(1): p. K25-K28.

5. D.J. Rowcliffe and G.E. Hollox, *Plastic flow and fracture of tantalum carbide and hafnium carbide at low temperatures.* Journal of Materials Science, 1971. **6**(10): p. 1261-1269.

6. R.H.J. Hannink, D.L. Kohlstedt, M.J. Murray, and D. Tabor, *Slip system determination in cubic carbides by hardness anisotropy.* Proceedings of the Royal Society of London. A. Mathematical and Physical Sciences, 1972. **326**(1566): p. 409-420.

7. A.S. Kurlov and A.I. Gusev, *Tungsten carbides.* Springer Ser. Mater. Sci, 2013. **184**: p. 34-6.

8. H.R. Huang, X.Z. Li, X. Liang, H. Nagaumi, H.Z. Fu, and D.M. Liu, *Nanocrystalline vanadium carbides as highly active catalysts on vanadium foils for high temperature hydrogen separation.* Separation and Purification Technology, 2023. **307**.

9. Y. Kumashiro and E. Sakuma, *The Vickers micro-hardness of non-stoichiometric niobium carbide and vanadium carbide single crystals up to 1500° C.* Journal of Materials Science, 1980. **15**(5): p. 1321-1324.

10. A. Aleman, H. Zaid, B.M. Cruz, K. Tanaka, J.M. Yang, H. Kindlund, and S. Kodambaka, *Room-temperature plasticity and size-dependent mechanical responses in small-scale B1-NbC(001) single-crystals.* Acta Materialia, 2021. **221**.

11. S. Kiani, C. Ratsch, A.M. Minor, J.M. Yang, and S. Kodambaka, *In Situ Transmission Electron Microscopy Observations of Room-Temperature Plasticity in Sub-Micron-Size TaC(100) and TaC(011) Single Crystals.* Scripta Materialia, 2014. **100**.

12. T. Glechner, R. Hahn, T. Wojcik, D. Holec, S. Kolozsvári, H. Zaid, S. Kodambaka, P.H. Mayrhofer, and H. Riedl, *Assessment of ductile character in superhard Ta-C-N thin films.* Acta Materialia, 2019. **179**: p. 17-25.

13. M.D. Uchic, P.A. Shade, and D.M. Dimiduk, *Plasticity of Micrometer-Scale Single Crystals in Compression.* Annual Review of Materials Research, 2009. **39**(1): p. 361-386.

14. S. Korte and W.J. Clegg, *Discussion of the dependence of the effect of size on the yield stress in hard materials studied by microcompression of MgO.* Philosophical Magazine, 2011. **91**(7-9): p. 1150-1162.

15. C. Zhou, I.J. Beyerlein, and R. LeSar, *Plastic deformation mechanisms of fcc single crystals at small scales.* Acta Materialia, 2011. **59**(20): p. 7673-7682.

CHAPTER 5

Plasticity and Mechanical Responses in TaC Single-Crystals

5.1 Introduction

Tantalum carbide (TaC) is probably one of the most commonly used TMCs in a variety of important technical applications: as an alloying addition to tungsten carbide-cobalt cemented carbides [1], to inhibit tungsten carbide grain growth, and with tungsten carbide-cobalt cutting tools to improve the cutting characteristics, shock resistance, high-temperature hardness, cratering, and wear and oxidation resistance [2]. With its extremely high melting temperature of T_m ~ 4236 K, TaC is an attractive candidate for applications in aerospace, structural, and as protective coatings [1, 3]. It is also attractive as an Ohmic contact in high-temperature electronics [4] and as a spectrally selective coating for solar thermal absorbers [5].

In this Chapter, I present results from *in situ* SEM-based microcompression of TaC(110) and TaC(111) single-crystals. The choice of these two particular orientations is motivated by Kiani and co-workers' earlier studies [6] on *in situ* TEM-based compression tests conducted on ~ 200-500 nm size TaC(001) and TaC(110) single-crystalline pillars.

5.3 Results

5.3.1 TaC(110)

Figures 5.1 (a-c) show representative SEM images from the bulk TaC(110) single crystal of three sub-micron pillars, before (top panel) and after (bottom panel) compression. The SEM images are 10°-tilted views of the pillars with top diameters $D \approx$ a) 0.27 μm, b) 0.41 μm, and c)

0.70 μm. The height of the pillars and their average diameters do not noticeably change upon compression based on these images, i.e. it is not visually apparent that the pillars deformed plastically. The three sets of pillars reach a displacement of 150-175 nm before fracturing. This behavior is typical of two out of four pillars with average $D \approx 0.27$ μm, three out of five pillars with $D \approx 0.41$ μm, and three out of five pillars with $D \approx 0.69$ μm. The other six pillars deformed slightly followed by fracture and one pillar was omitted from compression testing due to an artifact. For the unfractured pillars their estimated plastic strains are between 3 and 5% for $D \approx 0.27$ μm, 1% for $D \approx 0.41$ μm, and 0.3 and 2% for $D \approx 0.69$ μm. Here the smallest pillars seem to experience the greatest amount of plastic deformation based on the σ vs δ curves and the estimated strain values. The unfractured pillars of the $D \approx 0.41$ and 0.69 μm sets could have been further compressed. However, the goal was to preserve the pillars to capture and characterize their slip systems, thereby limiting the extent of compression.

Engineering stress vs. displacement data obtained during the *in situ* compression of the 14 pillars are plotted in Figures 5.1 (d), (e), and (f) for their corresponding sizes. The σ-δ data corresponding to the pillars in Figures 5.1 (a) – (c) are highlighted using red, green, and blue colors, respectively. In the initial stages of loading and the σ-δ profiles, I observe a linear elastic behavior, and the majority of the pillars undergo elastic deformation: δ increases linearly with increasing σ up to the yield point, σ_y, followed by a smooth transition to non-linear plastic deformation for the smaller set of pillars with diameters up to $D \sim 0.27$ μm while a transition to the non-linear plastic deformation can be seen but does not fully developed for the pillars having diameters $D \sim 0.41$ μm, and a non-linear plastic deformation region is not observed for the largest pillars with diameters $D \sim 0.69$ μm. The largest pillars have sudden drops in σ with a

large displacement increase, indicating a large slip event or sudden fracture i.e., the pillars exhibit brittle behavior.

The yield strength σ_y of the 14 pillars is extracted from the σ vs δ curves in Figures 5.1 (d) – (f) and plotted as a function of *D* in Figure 5.2. From the profiles, the observed trend is that σ_y increases as the *D* decreases, from 17.6 ± 4.1 GPa for pillars with $D \approx 0.69$ μm to 22.1 ± 0.3 GPa for pillars with $D \approx 0.27$ μm. One data point in the smallest diameter set is missing from the trend. The pillar was omitted from compression testing due to an artifact and eliminated from the data set.

To further characterize the observed behavior of size dependent plastic deformation, the compressed pillars were imaged with electron microscopy. Figures 5.3 (a) – (c) are typical higher resolution SEM images obtained after compression of the same representative pillars from Figure 5.1 with $D \approx$ 1(a) 0.27 μm, 1(b) 0.41 μm, and 1(c) 0.70 μm. In Figure 5.3 all of the pillars exhibited localized plastic deformation shown by the slip bands at the top surface. Most of the pillars, if not all in each set that were tested, show clear evidence of slip and only one or two in each set fractured. Dashed red, green, and blue lines, respectively, in Figures 5.3 (a), (b), and (c) highlight the orientations of the slip bands with respect to the [110] pillar axes, where the angle shown is the angle between normal to the slip trace and the pillar axis and equivalently the angle between pillar axis normal surface and the slip trace. In Figures 5.3 (a) – (c), the shear bands are oriented at ~ 35° and ~ 45°. Since each pillar axis is [110], the possible slip planes that are orientated at 35° and 45° with respect to the pillar axis belong to {111} and {001}, respectively. Based on this result, the operating slip systems in these pillars are $\{111\}\langle 1\bar{1}0\rangle$ and $\{001\}\langle 1\bar{1}0\rangle$. The range of pillar sizes help to observe or exclude if a transition in slip system may occur based

on the size of the crystal. Since two unique slip systems have been captured in different sizes, perhaps a transition does occur and will be addressed in the discussion section.

5.3.2 TaC(111)

Figure 5.4 shows representative SEM images from the bulk TaC(111) single crystal of three sub-micron pillars, before (top panel) and after (bottom panel) compression. The SEM images are 10°-tilted views of the pillars with top diameters $D \approx$ a) 0.26 μm, b) 0.42 μm, and c) 0.67 μm. From these images, only the height of the pillar in Figure 5.4(b) noticeably decreased, while the other two pillars, in Figures 5.4 (a) and (c), and their average diameters do not noticeably change upon compression based on these images, i.e. it is not visually apparent that the pillars deformed plastically. However, a more common observation of all the pillars is the formation of slip bands at the top section and continuing across the body of the pillars i.e., the pillars experienced plastic deformation by large slip bands, and can be seen in Figure 5.4 (a) and (c). This behavior is typical of all five pillars with $D \approx 0.27$ μm and one out of five with $D \approx 0.41$ μm, and three out of five with $D \approx 0.67$ μm. The other pillars deformed to a small extent and fractured. For the unfractured pillars their estimated plastic strains are between 1 and 8% for $D \approx 0.27$ μm, 20% for $D \approx 0.41$ μm, and 2 and 4% for $D \approx 0.67$ μm. Here the smallest pillars seem to experience the greatest amount of plastic deformation based on the σ vs δ curves. The one pillar in the $D \approx 0.41$ μm group, has a rather large, estimated strain (~20%) due to a partial fracture resulting in the loss of about half of the top surface area of the pillar. This sudden application of a large load on a reduced area (~4x stress) created a sudden displacement burst and further deformation of the pillar as shown in Figure 5.6(b). The other pillars could have been further

compressed; however, the goal was to preserve the pillars to capture and characterize their slip systems, limiting the extent of compression.

Engineering stress vs. displacement data obtained during the *in situ* compression of all 15 pillars are plotted in Figure 5.4 (d), (e), and (f) for their corresponding sizes. The σ-δ data corresponding to the pillars in Figure 5.4 (a), (b), and (c) are highlighted using red, green, and blue colors, respectively. During the initial stages of loading, the profiles indicate a linear elastic behavior: δ increases linearly with increasing σ up to the yield point σ_y, followed by a smooth transition to non-linear plastic deformation for the smaller set of pillars with $D \approx 0.27$ μm and $D \approx 0.41$ μm while a transition to the non-linear plastic deformation can be seen but does not fully develop for the larger set of pillars with $D \approx 0.67$ μm. Some of the largest pillars also have sudden drops in σ with a large displacement increase following their undeveloped transition to plastic deformation, indicating a large slip event or sudden fracture i.e., these pillars also exhibit brittle behavior. At $\sigma > \sigma_y$ I observe the following: 1) small and large frequent drops in σ due to displacement bursts, where the amplitudes appear to remain constant with decreasing *D* and 2) the rate of strain hardening appears to increase with decreasing *D*.

The yield strength σ_y of the 15 pillars is extracted from the σ vs δ curves in Figure 5.4 (d) – (f) and plotted as a function of *D* in Figure 5.5. From the profiles, the observed trend is that σ_y increases as the *D* decreases, from 13.6 ± 1.7 GPa for pillars with $D \approx 0.67$ μm to 15.3 ± 4.6 GPa for pillars with $D \approx 0.27$ μm. The smallest diameter set includes two values that are much lower than the others and decreases the average yield strength and increases the standard deviation. If the two values are omitted the average and standard deviation is 18.6 ± 1.1 GPa for pillars with $D \approx 0.27$ μm. No anomalies were observed, and the low values can be attributed to variations in

the dislocation density and defect variations in the pillars. All pillars are included in the data set for the (111) surface orientation.

To further characterize the observed behavior of size dependent plastic deformation, the compressed pillars were imaged with electron microscopy. Figures 5.6 (a), (c), and (d) are typical higher resolution SEM images obtained after compression of the same representative pillars from Figure 5.4 with $D \approx$ (a) 0.26 μm, (b) 0.42 μm, and (c) 0.67 μm. Figures 5.6 (d) and (e) are more pillars having $D \approx 0.27$ μm and $D \approx 0.40$ μm, respectively. In Figure 5.6 all of the pillars exhibited plastic deformation shown by the slip bands at the top surface and across the body of the pillars. The pillar in Figure 5.6(a) also has multiple slip bands across the body and is a great example for the comparison of size differences. All of the pillars that were tested show clear evidence of slip and five pillars fractured, three in the $D \approx 0.41$ μm set and two in the $D \approx$ 0.67 μm set. Dashed red, green, and blue lines, respectively, in Figures 5.6 (a) and (d), (b) and (e), and (c) highlight the orientations of the slip bands with respect to the [111] pillar axes, where the angle shown is the angle between normal to the slip trace and the pillar axis and equivalently the angle between pillar axis normal surface and the slip trace. Following the same procedure of measuring the angle of the slip band as in Figure 5.3, I can identify the slip system for each pillar. In Figure 5.6(a) there are several parallel shear bands across the body of the pillar, many are faint, and one is located by a red arrow. Also, in Figure 5.6(a) a slip band is seen at the top surface of the pillar extending to the backside, shown by a red arrow, and is responsible for shearing off the majority of the top of the pillar. The largest shear band shown is oriented at ~ 54°, indicating a (001) slip plane. In Figure 5.6(b) a large shear band can be seen from the top surface and across the top portion of the pillar at ~ 54°, indicating a (001) slip plane in the ⟨110⟩ slip direction. In Figure 5.6(c) I observe a large slip band across the entire body of the pillar at ~

70°, indicating that the (111) slip plane is active. In Figure 5.6(d) three parallel slip bands are present across the body of the pillar at ~ 70°, indicating a (111) slip plane, and a separate set of multiple slip bands are visible and indicated by red arrows. In Figure 5.6(e) I observe two different orientations of the slip bands. A large shearing of the top portion of the pillar at ~ 70° is present and several parallel shear bands are present at ~ 54° located by the green arrows, indicating that the (111) and (001) respective slip planes, are active.

With the assumption that $\langle 1\bar{1}0 \rangle$ is the slip direction, generally expected in B1 crystals, these results indicate the operation of the $\{001\}\langle 1\bar{1}0 \rangle$ and $\{111\}\langle 1\bar{1}0 \rangle$ slip systems. Furthermore, the range of pillar sizes help to observe that a common slip system, $\{111\}\langle 1\bar{1}0 \rangle$, occurs throughout the three sizes of crystals.

5.4 Discussion

While the operation of both $\{110\}\langle 1\bar{1}0 \rangle$ and $\{111\}\langle 1\bar{1}0 \rangle$ slip systems have been observed during microindentation of bulk TaC(001) and other group 5 TMC(001) single-crystals at liquid nitrogen temperature and room-temperature [7], I note that there are no reports for room-temperature compression of group 5 TMC crystals, of the activation of two slip systems, and on different crystal orientations with the exception of one. The previous report by Kiani et al. identified $\{110\}\langle 1\bar{1}0 \rangle$ as the only slip system during uniaxial compression of 001-oriented single-crystalline TaC pillars with $D < 0.5$ μm [6], while in 110-oriented Ta-C-N pillars, $\{111\}\langle 1\bar{1}0 \rangle$ is found to be the only active slip system [8]. The observed differences between my study and that of Kiani's TaC results may be due to differences in pillar sizes, crystal orientation variations, C-contents and loading rates. Here I have again observed the activation of multiple slip systems in two different crystal orientations of sub-micron pillars, identified two slip

systems within each crystal orientation, and the simultaneous activation of two slip systems within the same pillar.

During compression of the pillars, yielding occurred via slip either by one or a combination of the following descriptions: locally at the top surface, across the body of the pillar, and/or through multiple parallel slip bands creating multiple slip steps on the surface of the pillar. From the post compression morphology shown in Figures 5.3 (a) and (b), and Figures 5.6 (a), (d) and (e), it is apparent that I can observe localized deformation as shear bands on the top surfaces. In the pillars of Figure 5.3(c), and Figures 5.6 (a) - (e), I observe the shear bands across the body of the pillars. The observed behaviors are characteristic of plastic deformation that is typically observed in FCC bulk and microcrystals of metals [9]. The localized deformation behavior is typically observed in ionic crystals [10].

The explanation given for the NbC, and VC results partly applies to the TaC pillars. The number of dislocations and/or dislocation sources scales with pillar size. In smaller size pillars ($D \approx 0.27$ μm), the number of dislocations (and/or sources) within the pillar is expected to be low and plastic deformation is likely to be controlled by the surface nucleation of dislocations [11] along energetically the most favorable slip system. As a result, slip events are expected to be finite and discontinuous resulting in displacement bursts with larger amplitudes and higher yield strength. With increasing pillar size, both surface nucleation and multiplication of internal dislocations lead to higher number of dislocations and the activation of a second slip system. However, this results in less plastic deformation perhaps because of dislocation entanglements, thereby creating brittle behavior with lower yield strength. For the TaC(110) crystal orientation, inherent in my model is the speculation that the $\{001\}\langle 1\bar{1}0\rangle$ and $\{111\}\langle 1\bar{1}0\rangle$ slip systems are dominant in relatively smaller and large-size crystals, respectively. In TaC(111) a combination of

two slip systems can be active depending on size. For example, the $\{001\}\langle 1\bar{1}0\rangle$ and $\{111\}\langle 1\bar{1}0\rangle$ slip systems are active for the two sets of pillars with $D \approx 0.27$ μm and 0.41 μm, and only the $\{111\}\langle 1\bar{1}0\rangle$ slip system is active for the set of pillars with $D \approx 0.67$ μm. Also, the $\{111\}\langle 1\bar{1}0\rangle$ slip system is active for all sizes and is therefore considered the dominant slip system.

These observations indicate that the two TaC orientations of 110 and 111 are experiencing plasticity or brittle behavior depending on their size. To elaborate, the 110 oriented pillars can experience plastic deformation and brittle behavior as characterized by their σ-δ curves in Figures 5.1 (d-f). They are considered brittle for larger diameters with the ability to sustain plastic deformation with smaller diameters $D \approx 0.27$ μm. The TaC(111) pillars can also experience plastic deformation and brittle behavior as characterized by their σ-δ curves in Figures 5.4 (d-f). The TaC(111) pillars are considered plastic with the ability to sustain further plastic deformation with decreasing diameters and are relatively brittle for larger diameters $D \approx$ 0.67 μm. Additionally, it is interesting to note that the σ-δ curves of the larger pillars are indicating a transitional behavior. At the end of the curves a slight bending is visible, which is indicative of a transition to the non-linear plastic deformation. Following this trend for pillars larger than $D \approx 0.67$ μm, I would expect that the pillars would behave in a brittle manner. And with further larger sizes, I would also expect the σ-δ behavior of both crystal orientations to eventually merge with that of a TaC(110) or TaC(111) bulk material.

The possibility that a transition in slip system may occur based on the size of the pillar and crystal orientation was explored here in the TaC crystals. This is supported for the 110 orientation because I observe only one slip system, $\{001\}\langle 1\bar{1}0\rangle$, for the smallest pillars ($D \approx 0.27$ μm) and another slip system for larger pillars of $D \approx 0.41$ and 0.69 μm. Perhaps a transitional

size exists between the two sizes ($D \approx 0.27 - 0.41$ μm) where two slip systems are activated followed by the activation of only the second slip system in the larger pillars for $D \geq 0.41$ μm. The 111 orientation has the most interesting behavior because the same two slip systems are active within two different pillar sizes of $D \approx 0.27$ and 0.41 μm. Here, a transition seems to be occurring in the smaller pillars with $D \approx 0.27$ and 0.41 μm where two slip systems, $\{001\}\langle 1\bar{1}0\rangle$ and $\{111\}\langle 1\bar{1}0\rangle$, are active followed by the activation of only one slip system, $\{111\}\langle 1\bar{1}0\rangle$, in the larger pillars of $D \approx 0.67$ μm. It is interesting to note that since a transition seems to be occurring at $D \approx 0.27$ μm perhaps then at smaller pillar diameters only the (001) slip plane could be active. Furthermore, the (111) slip plane is present in all three sizes and is contributing to the plastic nature of the 111 oriented pillars as seen in Figure 5.6. The observation of the plasticity increasing with decreasing diameter can be attributed to the presence of two slip systems allowing for extended deformation. In the larger diameters only one slip system is active thereby limiting the amount of plastic deformation compared to the smaller pillars. As mentioned in the previous paragraph, because of the presence of only one slip system at larger sizes, for both crystal orientations, I would expect that the pillars would behave in a brittle manner and with further larger sizes, the mechanical behaviors eventually merging with that of the bulk TaC(110) or TaC(111) material.

Figure 5.7 compares the mechanical yield strengths of the two pillar orientations. Clearly, for all orientations there is an increase in yield strength at different rates for each orientation as the diameter is decreased. Here, the strength of the 111 orientation increases at a faster rate and is considered the “soft” orientation, relatively speaking, because earlier it was described that the 111 orientation experienced the most plastic deformations. The strength of the 110 orientation increases at the slowest rate and is considered the “hard” orientation because earlier it was stated

that the 110 orientation did not experience plastic deformations until reaching the smallest pillar diameters and was described as brittle. Specifically, the 111 orientation has the combination of allowing for plastic deformation and higher yield strengths, approaching the values of the 110 orientation for the smallest diameters, making it an attractive orientation for mechanical applications.

5.5 Conclusion

The micromechanical responses of TaC with 110 and 111 orientations were observed and analyzed to characterize each and determine their active slip systems. *In situ* SEM based compression of TaC(110) and TaC(111) is carried out on pillars with sub-micrometer size diameters. The results revealed that the pillars deform plastically with moderate strains, compared to NbC and VC, and diameter-dependent yield strengths that increase with decreasing diameter. Interestingly, the pillars exhibit more plastic deformation as the diameter is decreased. From the SEM images, I have identified the operation of two slip systems dependent on the crystal orientation and pillar diameter, and also the observation of a transition in slip system for both orientations. Based on these results, I suggest the relatively more brittle TaC(110) is a result of only one active slip system per size while the moderate plasticity in TaC(111) crystals at room-temperature is a direct consequence of the simultaneous presence of two slip systems. These results again support the exciting possibility of designing refractory TMCs with superior plasticity by optimizing the grain size, orientations, and composition that promotes the activation of single or multiple desired slip systems.

5.6 Figures

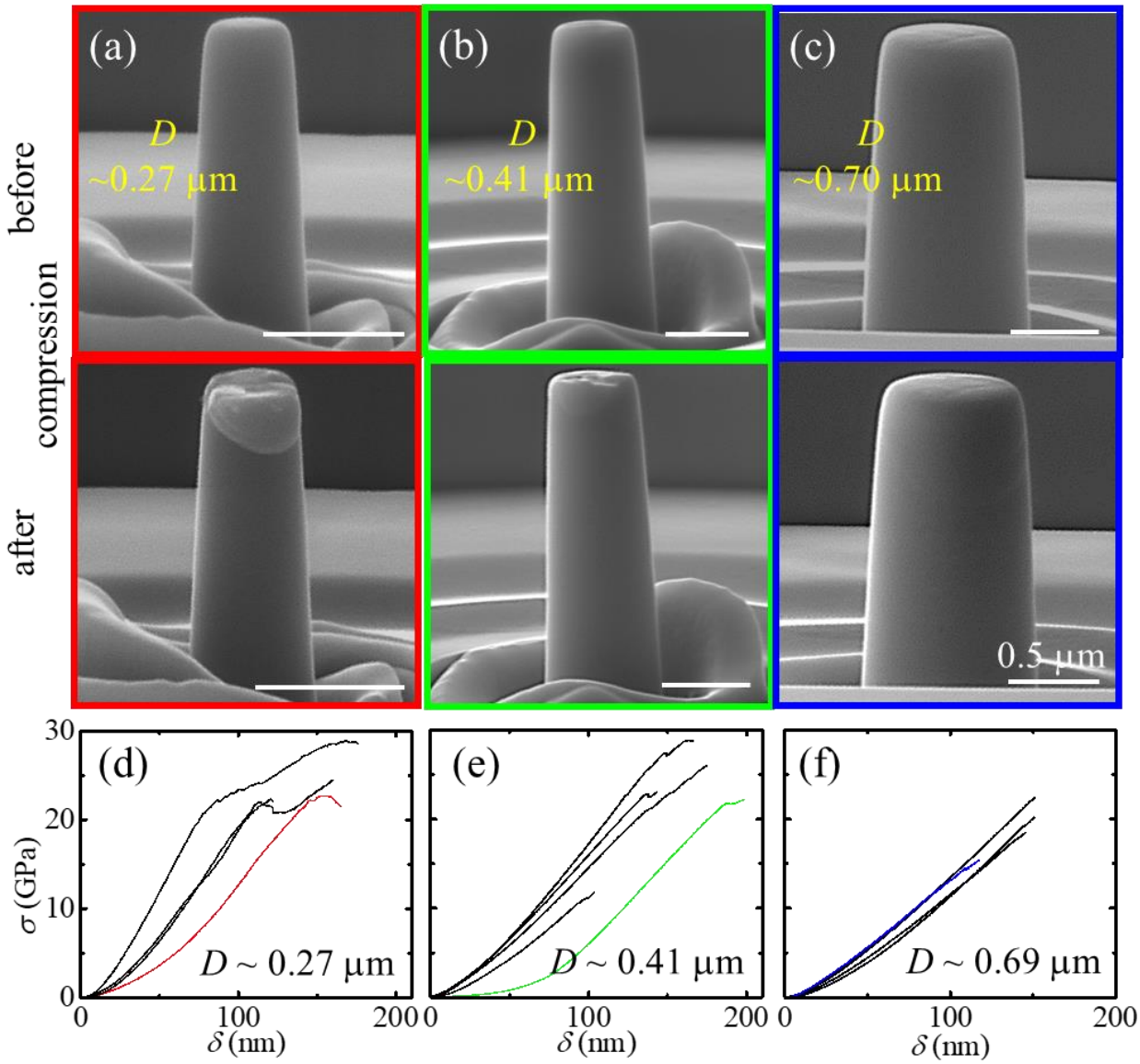

Figure 5.1: (a-c) Representative SEM images acquired from the bulk TaC(110) with pillars of top diameters D = a) 0.27 μm, b) 0.41 μm, and c) 0.70 μm before (top panel) and after compression (bottom panel). (d-f) Plots of engineering stress (σ) vs. displacement (δ) data obtained during *in situ* compression of three sets of pillars with average D of (d) 0.27 μm, (e) 0.41 μm, and (f) 0.69 μm. The $\sigma(\delta)$ data corresponding to the pillars in (a), (b), and (c) are shown using red, green, and blue curves, respectively.

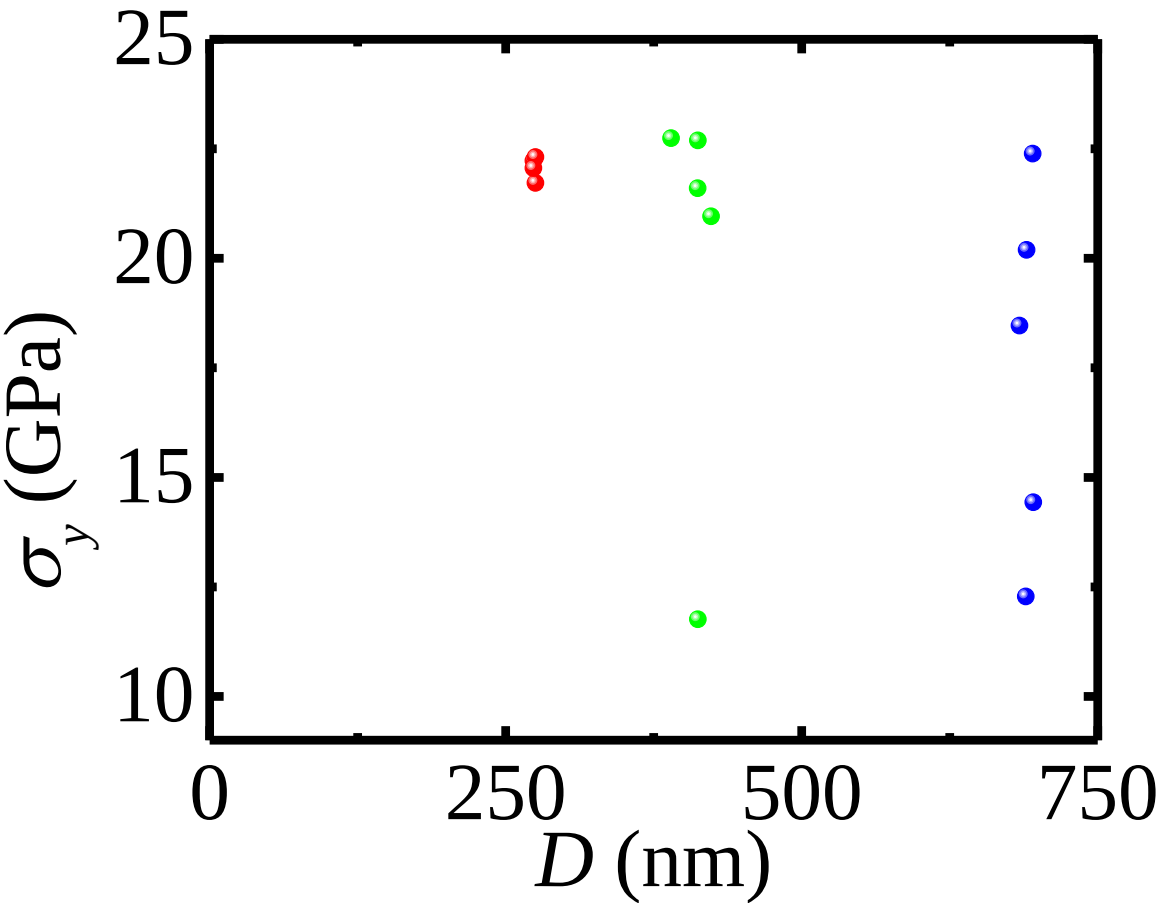

Figure 5.2: Plot of yield strengths σ_y vs. D, extracted from compression tests of all TaC(110) pillars from Figure 5.1, ranging in diameter from 0.27 to 0.70 μm.

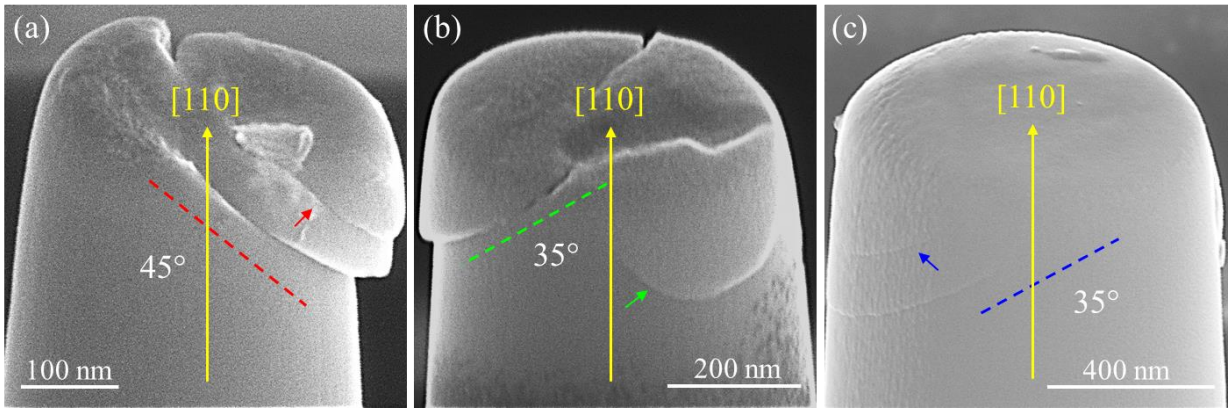

Figure 5.3: (a-c) Typical SEM images (60°-tilt) acquired after the compression of three different TaC(110) pillars with $D \approx$ (a) 0.27 μm, (b) 0.41 μm, and (c) 0.70 μm. Dashed red, green, and blue lines, respectively, in (a), (b), and (c) highlight the orientations of the slip bands with respect to the [110] pillar axes, where the angle shown is the angle between normal to the slip trace and the pillar axis and equivalently the angle between pillar axis normal surface and the slip trace. Note that in the figures there are other slip traces present on the surface of the pillars indicated by the arrows.

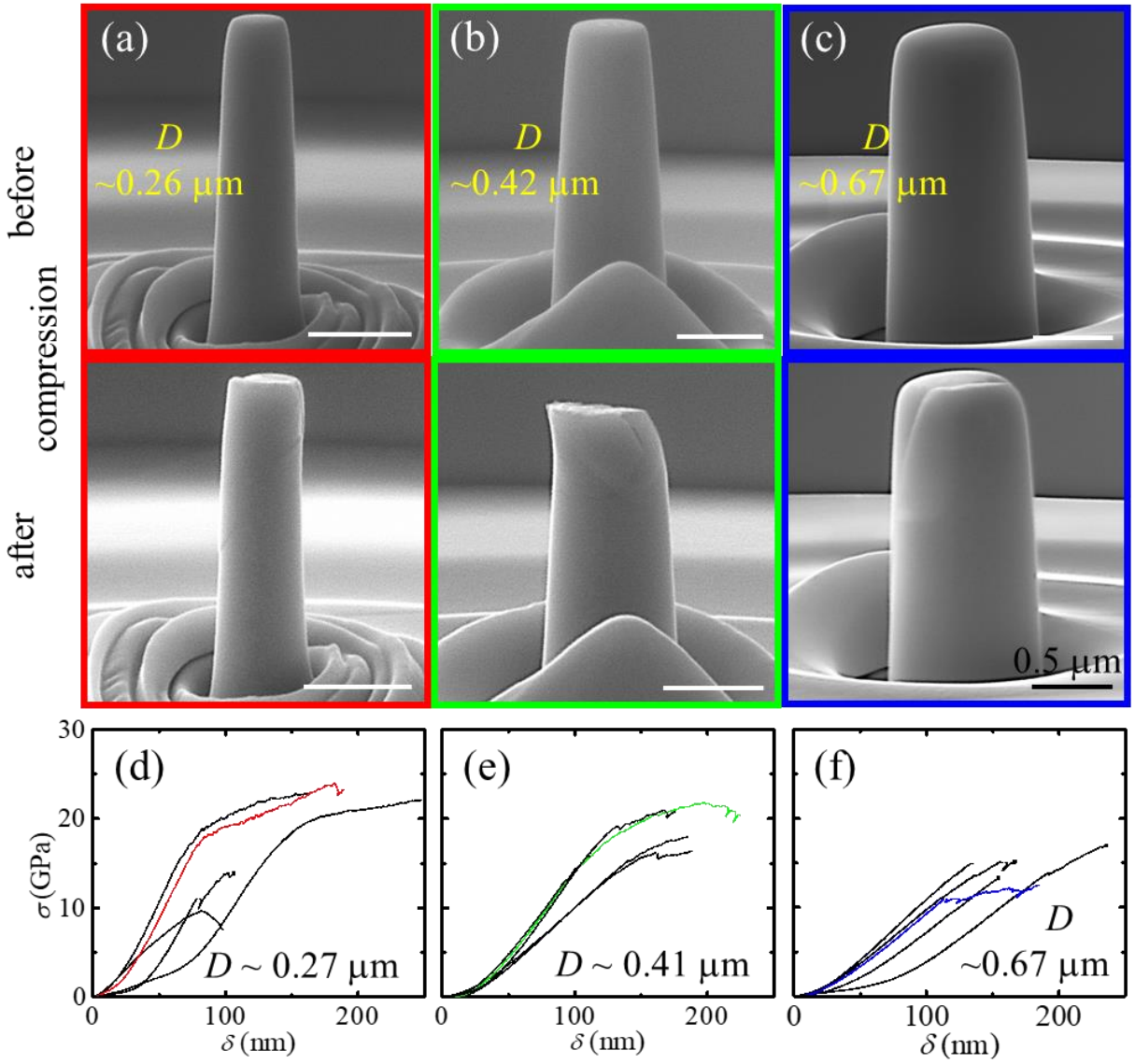

Figure 5.4: (a-c) Representative SEM images acquired from the bulk TaC(111) with pillars of top diameters D = a) 0.26 μm, b) 0.42 μm, and c) 0.67 μm before (top panel) and after compression (bottom panel). (d-f) Plots of engineering stress (σ) vs. displacement (δ) data obtained during *in situ* compression of three sets of pillars with average D of (d) 0.27 μm, (e) 0.41 μm, and (f) 0.67 μm. The $\sigma(\delta)$ data corresponding to the pillars in (a), (b), and (c) are shown using red, green, and blue curves, respectively.

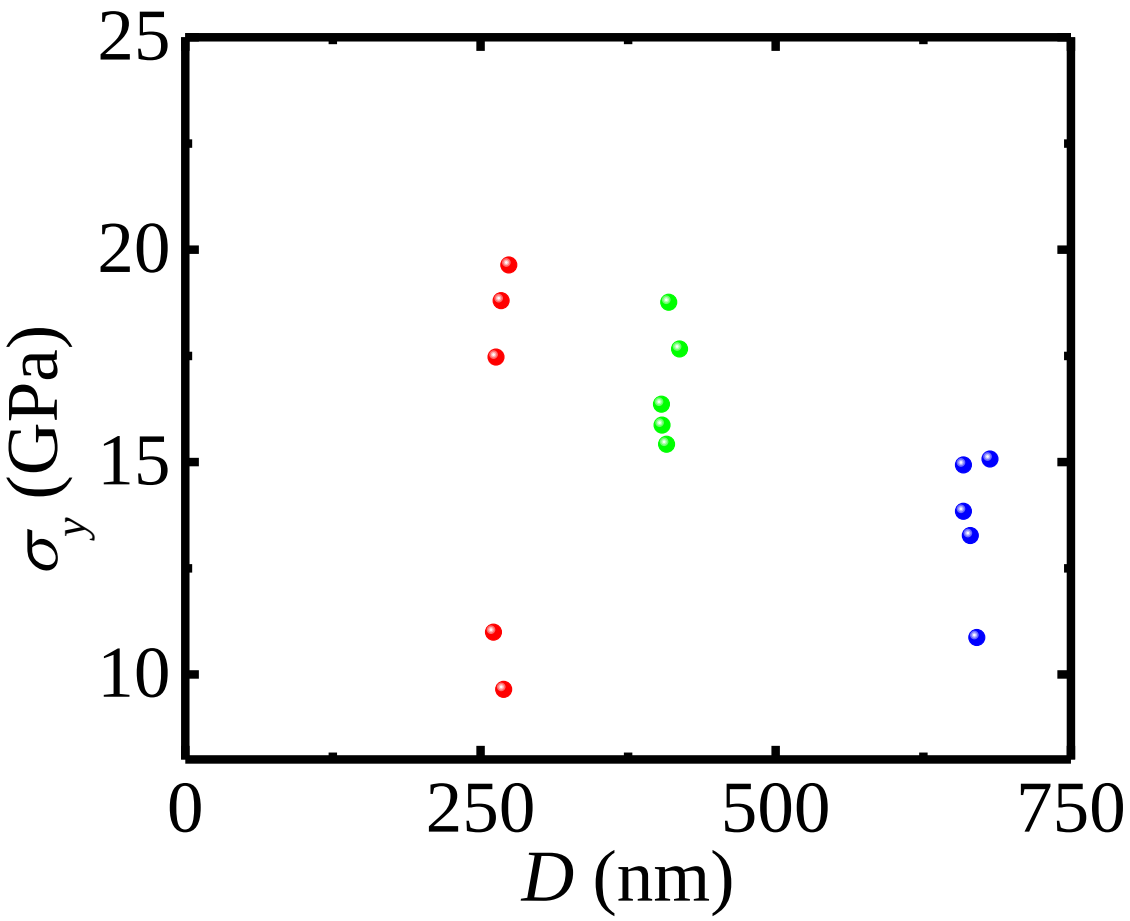

Figure 5.5: Plot of yield strengths σ_y vs. D, extracted from compression tests of all TaC(111) pillars from Figure 5.4, ranging in diameter from 0.26 to 0.68 μm.

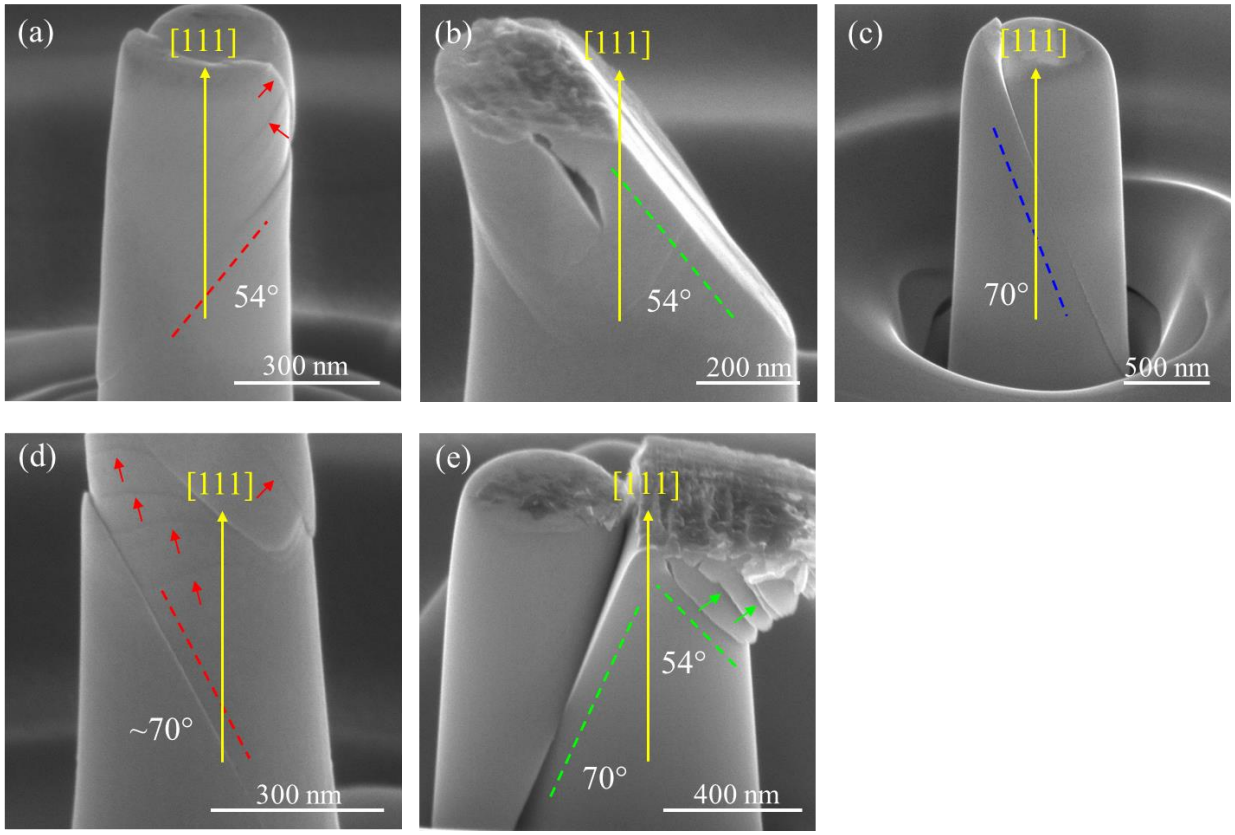

Figure 5.6: (a-e) Typical SEM images (60°-tilt) acquired after the compression of five different TaC(111) pillars with $D \approx$ (a) 0.26 μm, (b) 0.42 μm (c) 0.67 μm, (d) 0.27 μm, and (e) 0.40 μm. Dashed red, green, and blue lines, respectively, in (a) and (d), (b) and (e), and (c) highlight the orientations of the slip bands with respect to the [111] pillar axes, where the angle shown is the angle between normal to the slip trace and the pillar axis and equivalently the angle between pillar axis normal surface and the slip trace. Note that in (d) there are several faint slip traces present on the surface of the pillar indicated by the red arrows.

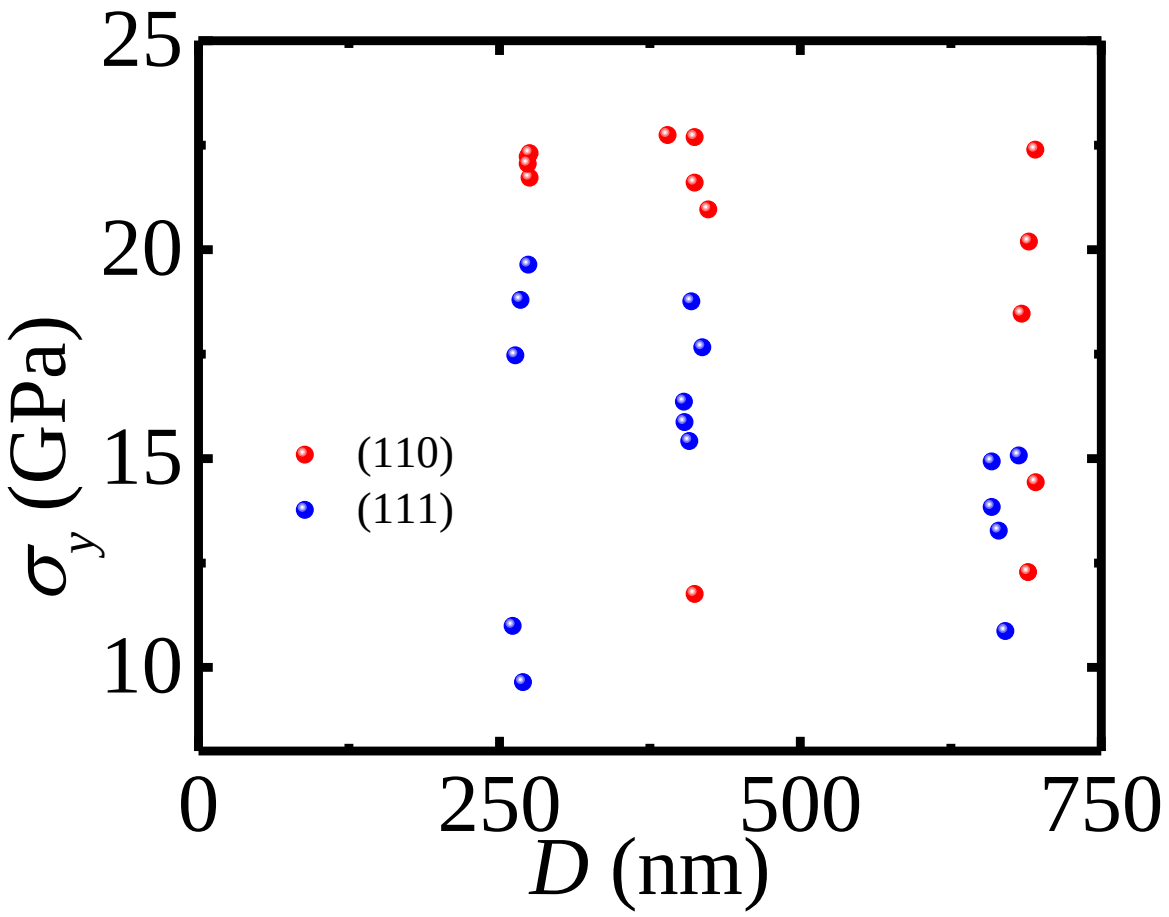

Figure 5.7: Plot of yield strength σ_y vs. D, summarizing all compression tests of TaC (110) and (111) pillars ranging in diameter from 0.27 to 0.70 μm from Figures 5.2 and 5.5.

References

1. L.E. Toth, *Transition metal carbides and nitrides*. 1971, New York: Academic Press.

2. H.O. Pierson, *Handbook of Refractory Carbides and Nitrides: Properties, Characteristics, Processing, and Applications*. 1996: William Andrew Publishing/Noyes.

3. W.S. Williams, *Transition-metal carbides.* Progress in Solid State Chemistry, 1971. **6**: p. 57-118.

4. R.D. Vispute, S. Hullavarad, A. Luykx, D. Young, S. Dhar, T. Venkatesan, K.A. Jones, T.S. Zheleva, M. Ervin, and M. Derenge, *Epitaxy and recrystallization kinetics of TaC thin films on SiC for high temperature processing of semiconductor devices.* Applied Physics Letters, 2007. **90**(24).

5. P. Kondaiah, K. Niranjan, S. John, and H.C. Barshilia, *Tantalum carbide based spectrally selective coatings for solar thermal absorber applications.* Solar Energy Materials and Solar Cells, 2019. **198**: p. 26-34.

6. S. Kiani, C. Ratsch, A.M. Minor, J.M. Yang, and S. Kodambaka, *In Situ Transmission Electron Microscopy Observations of Room-Temperature Plasticity in Sub-Micron-Size TaC(100) and TaC(011) Single Crystals.* Scripta Materialia, 2014. **100**.

7. R.H.J. Hannink, D.L. Kohlstedt, M.J. Murray, and D. Tabor, *Slip system determination in cubic carbides by hardness anisotropy.* Proceedings of the Royal Society of London. A. Mathematical and Physical Sciences, 1972. **326**(1566): p. 409-420.

8. T. Glechner, R. Hahn, T. Wojcik, D. Holec, S. Kolozsvári, H. Zaid, S. Kodambaka, P.H. Mayrhofer, and H. Riedl, *Assessment of ductile character in superhard Ta-C-N thin films.* Acta Materialia, 2019. **179**: p. 17-25.

9. M.D. Uchic, P.A. Shade, and D.M. Dimiduk, *Plasticity of Micrometer-Scale Single Crystals in Compression.* Annual Review of Materials Research, 2009. **39**(1): p. 361-386.

10. S. Korte and W.J. Clegg, *Discussion of the dependence of the effect of size on the yield stress in hard materials studied by microcompression of MgO.* Philosophical Magazine, 2011. **91**(7-9): p. 1150-1162.

11. C. Zhou, I.J. Beyerlein, and R. LeSar, *Plastic deformation mechanisms of fcc single crystals at small scales.* Acta Materialia, 2011. **59**(20): p. 7673-7682.

CHAPTER 6

Further Discussions

As mentioned in the introduction of this thesis, TMCs have an interesting combination of properties that span across the ceramic and metallic families. The reason for their hybrid properties can be best explained by considering many factors including their chemical bonding, composition, and their operating temperature. Each factor can vary their properties by activating or suppressing mechanisms that are inherent in their microstructure. The following sections are just a few, more apparent, and readily studied factors regarding the behavior of TMCs. These sections are by no means an extensive presentation of their properties and readily become beyond the scope of this study. I am presenting these topics here because it aides the reader to understand the bigger picture regarding the mechanical properties of TMCs.

6.1 Chemical Bonding

Chemical bonding is such an important aspect to better understand the behavior of TMCs that it is worth mentioning here. Understanding their behavior will allow for designing the TMCs appropriately and to prevent catastrophic failures.

6.1.1 Covalent, Ionic, Metallic

The chemical properties of TMCs have been studied through simulations [1] and mechanical experiments of microhardness [2] and bending [3], at room and high temperatures. TMCs owe their superior high temperature strengths and extreme hardness to their covalent and metallic bonding [4]. It is now well known that covalent bonding is dominant at low temperatures over their metallic bonding [2, 3, 5]. The carbon 2p states mix with the metal 3d or

4d atomic states near the Fermi energy to create the covalent component [1] while the ionic contribution results from partial electron transfer from metal to carbon while forming the compound. The metallic component likely includes d band bonding typical of transition metals, resulting from partial filling of the atomic d states while forming the compound [5]. The metal orbitals are likely of the d^2sp^3 hybridization because the typical octahedral grouping of the metal atoms centered on the carbon atom has six bonds to the six corners of the octahedron, favoring the M-C bond [6]. These studies indicate that the carbides intrinsically have a high Peierls stress that resist the dislocation motion giving them superior mechanical properties. Therefore, if the chemical bonding is altered, then it can change their properties. Just how the TMCs can be composed or altered to exhibit its hard ceramic-like behavior or ductile metallic property will be briefly discussed in the following sections.

6.1.2 Electron Screening

Within the chemical bonding present in the microstructure there is a particular feature that occurs when too many electrons are present and also alters the properties of the carbides. As the carbon content is increased, so do the number of electrons entering the metallic bonding orbitals and provide further strength to the carbide in the form of covalent bonding. A general approach to the electronic structure of transition metals and their compounds suggests that an optimum d band number of about 6 electrons is obtained for compounds of greatest stability [7]. If the number of electrons exceeds the optimum in the bonding orbitals, they begin to fill the anti-bonding orbitals causing a decrease in strength in some of the TMCs [8] and especially in the G5 carbides as shown in Figure 1.1.

The weakening of the carbides is described by [2] as an electron screening of the covalent bonding between the metal and carbon atoms. The dominant contribution to the weakening is a reduced effectiveness of the hybridized orbitals that form the covalent bonds by the efficient screening of the low effective mass (high mobility) s-electrons. With increasing temperature, the number of s-electrons and screening increases.

The electron screening effect is a deterioration of the chemical bonding and affects the mechanical and electrical properties of the TMCs. Interestingly, the electron screening is temperature and compositionally dependent and affects the G5 carbides.

6.2 Temperature (DBTT)

The operating temperature also influences the mechanical properties of the carbides. At low temperatures, the {110}<110> is the dominant slip system where the carbides are considered brittle while at high temperatures (> $0.3T_m$) the {111}<110> slip system is more dominant where they behave ductile [2]. This is a transition from covalent to metallic cohesion as temperature is raised. Therefore, there exists an approximate temperature where a transition takes place and is called the ductile-brittle transition temperature (DBTT). A decrease in the DBTT might also be expected as the carbon content is decreased [9].

Furthermore, it was stated in the introduction that group 4 and 5 TMCs have similar slip system transitions that are temperature dependent. These temperature dependent slip systems are a consequence of the change in the chemical bonding controlling the strength. The DBTT is also related to the view that deformation at higher temperatures is influenced by diffusion of the transition-metal [9].

6.3 Carbon-to-Metal Ratio (Composition)

The composition of the carbide is another factor to consider in designing the TMCs. It determines the microstructure and hence the mechanical and electrical properties. Another way to view the composition is through the vacancy concentration and is directly related to amount of carbon present in the carbide. Carbon vacancies can have short or long range order [9] affecting the microstructure along with the properties of the carbide [5, 6].

6.3.1 Critical composition

There is a composition to which the hardness and mechanical properties of the carbides are maximized and is dependent on the group of the transition-metal. Figure 1.1 shows the relationship between the carbon content and the hardness of the TMC. The niobium and tantalum -carbides are group 5 carbides that have a non-linear relationship while titanium, zirconium, and hafnium -carbides are group 4 carbides that exhibit a linear relationship. The group 5 carbides exhibit a maximum hardness at a carbon-to-metal ratio of $x \sim 0.83$ [10] which is the M_6C_5 phase. This phase can be considered a critical composition or optimum similar in effect to the maximum number of electrons allowed in the limited number of bonding orbitals. It seems that for group 5 carbides, adding more carbon (electrons) weakens the bonding by electron screening, and removing carbon weakens the bonding by reducing the amount of covalent bonds. Hence, at compositions higher or lower than $x \sim 0.83$ the hardness decreases as shown in Figure 1.1. Since the hardness is related to its strength, then the mechanical strength also decreases when the critical composition is offset from optimum.

6.3.2 Microstructure

The microstructure is dependent on the composition. From the phase diagrams of the carbides [6], it can be seen that as the atomic percent carbon is increased from approximately 40% the G4 carbides remain as substoichiometric carbides while increasing the atomic percent carbon beginning at approximately 30% the G5 carbides experience phase transformations in their microstructure [6, 10]. These phase transformations certainly affect their mechanical properties by increasing hardness and strength with an increase in carbon content as shown in Figure 1.1. Furthermore, as the phase changes, so do the active slip systems that determine its ductility [11].

6.4 Change of Slip System

The change of slip system can be described as a transition in the chemical bonding. For example, as temperature is increased the electrons within directional (covalent) bonding are thermally activated and can transition into less localized metallic states, effectively reducing the directionality and strength of the bonds.

6.5 Overall summary

The stress-displacement behavior of the pillars depends on the transition metal, pillar size, and crystal orientation.

The NbC(001) results revealed that the pillars (crystals) with sub-micrometer size diameters deform plastically with large strains and diameter-dependent yield strengths that increase with decreasing diameter. The largest pillars were able to sustain extended plastic

deformation without fracturing. NbC revealed itself to be the most plastic of the G5 TMCs regardless of the crystal size and orientation.

The VC results revealed that the 001-oriented pillars deform plastically with large strains and diameter-dependent yield strengths that increase with decreasing diameter. The 110 orientation is the hardest of the three because it does not exhibit plastic deformation and is described as brittle. The 111-oriented pillars also experience plastic deformation and are considered plastic with the ability to sustain further plastic deformation (but limited compared to VC(001) pillars) with larger diameters.

The TaC(110) pillars exhibited minimal local plastic deformation while TaC(111) pillars show relatively more plastic deformation, both with moderate strains compared to NbC and VC, and diameter-dependent yield strengths that increase with decreasing diameter. The interesting result is their increasing plasticity with decreasing size is contrary to those of NbC and VC, where the smaller pillars show less plastic deformation.

I find interesting that the Schmidt factor does not dictate and only indicates the occurrence of the preferred slip system. The secondary slip system can be activated alone, and the primary slip system can then be found within a different crystal size of the same TMC and orientation. The size dependence was explained by comparing the number of dislocations and sources available within the crystals. As the crystal size increases more dislocations and their sources are available and allows for plastic deformation. Less dislocations and their sources are available as the size decreases because they are readily annihilated to the free surfaces, then they have to be nucleated with larger forces to initiate or continue plastic deformation and hence described as a stronger pillar.

From literature reviews and in an attempt to describe the mechanical behavior of the TMCs on the atomic scale the following must be considered: The reduction of the covalent hardness to a metallic hardness over a wide temperature range is due to the thermal activation of electrons creating a transition in the chemical bonding. The transition creates changes in the carbide that are a result of the DBTT and a change in the slip systems. This relative softening is observed as ductile behavior that reduces the strength of the carbide. This DBTT serves as a reminder to designers of the dual nature of the carbides. Also, the composition of the carbides also affects their mechanical properties and the transition in the chemical bonding. These can be observed in the TMCs as phase and microstructural changes, carbon vacancies, and a change in the slip systems.

Much of the TMC properties are tunable making them open to design and hence very attractive for various applications. All of the variables discussed in this section must be considered when designing TMCs for the many potential applications in the aerospace, automotive, electronic, energy, and biomedical industries.

References

1. A. Neckel, *Recent investigations on the electronic structure of the fourth and fifth group transition metal monocarbides, mononitrides, and monoxides.* International Journal of Quantum Chemistry, 1983. **23**(4): p. 1317-1353.

2. R.H.J. Hannink, D.L. Kohlstedt, M.J. Murray, and D. Tabor, *Slip system determination in cubic carbides by hardness anisotropy.* Proceedings of the Royal Society of London. A. Mathematical and Physical Sciences, 1972. **326**(1566): p. 409-420.

3. W.S. Williams and R.D. Schaal, *Elastic Deformation, Plastic Flow, and Dislocations in Single Crystals of Titanium Carbide.* Journal of Applied Physics, 1962. **33**(3): p. 955-962.

4. L.E. Toth, *Transition metal carbides and nitrides*. 1971, New York: Academic Press.

5. W.S. Williams, *Physics of transition metal carbides.* Materials Science and Engineering: A, 1988. **105-106**: p. 1-10.

6. H.O. Pierson, *Handbook of Refractory Carbides and Nitrides: Properties, Characteristics, Processing, and Applications*. 1996: William Andrew Publishing/Noyes.

7. E. Dempsey, *Bonding in the refractory hard-metals.* The Philosophical Magazine: A Journal of Theoretical Experimental and Applied Physics, 1963. **8**(86): p. 285-299.

8. J.C. Grossman, A. Mizel, M. Côté, M.L. Cohen, and S.G. Louie, *Transition metals and their carbides and nitrides: Trends in electronic and structural properties.* Physical Review B, 1999. **60**(9): p. 6343-6347.

9. G.E. Hollox, *Microstructure and mechanical behavior of carbides.* Materials Science and Engineering, 1968. **3**(3): p. 121-137.

10. D.J. Rowcliffe and W.J. Warren, *Structure and properties of tantalum carbide crystals.* Journal of Materials Science, 1970. **5**(4): p. 345-350.

11. K. Tanaka, A. Aleman, H. Zaid, M.E. Liao, K. Hojo, Y. Wang, M.S. Goorsky, and S. Kodambaka, *Ultra-high vacuum dc magnetron sputter-deposition of 0001-textured trigonal α-Ta2C/Al2O3(0001) thin films.* Materialia, 2020. **13**: p. 100838.

CHAPTER 7

Future Work

7.1 Continuation

Throughout the text for each TMC tested here, it was stated that additional microcompression data from pillars of additional sizes within the sub-micrometer range and TEM characterization of the slip bands are needed to verify size-dependent activation of a specific slip system and to identify the likely existence of a transitional size, where both slip systems can be active. Ideally, this data can be obtained in a similar manner as here or can be obtained through a simulation study.

It remains to test the group 4 TMCs and their three low-index crystal orientations for comparison and characterization of their mechanical anisotropy. The 110 and 111 orientations remain to be tested for NbC. These orientations will allow for a comparison of their mechanical behavior. According to the results I have obtained here on the VC orientations, I predict the behavior of NbC will be similar. Mainly, the 001 orientation will be relatively softer and ductile, the 110 orientation will be stronger and relatively more brittle, and the 111 orientation will be a combination of both ductile and strong.

Many facets affecting the mechanical properties of the group 4 and 5 TMCs can be studied to continue the work. The most important facets for each transition metal are its composition, crystal orientation, pillar size, and temperature. Many of these can be controlled by the user to design the experiment and create a systematic study of the carbide of choice.

7.2 Recommendations

A difficult task to achieve is to determine the dislocation densities of each crystal to determine their role in the microstructure and on the plastic behavior of the transition metals.

The group 4 TMCs can also be studied using microcompression to determine their anisotropic mechanical behaviors, i.e., yield strength, extent of plasticity, and deformation mechanisms, and then compare with those of the G5 TMCs. In addition, these further studies are required to compare the group 4 and 5 TMCs based on similar location in the periodic table, composition, crystal orientation, pillar size, and temperature. Much knowledge will be obtained to further understand their mechanical properties to aid and expand their use in technical applications.